Chemical Engineering Journal 507 (2025) 160039

Contents lists available at ScienceDirect

Chemical Engineering Journal

journal homepage: www.elsevier.com/locate/cej

Nanoparticle formation in the boundary layer of burning iron microparticles: Modeling and simulation

Bich-Diep Nguyen [a], Arne Scholtissek [a,*], Tao Li [b], Daoguan Ning [b]
Oliver Thomas Stein [c], Andreas Dreizler [b], Christian Hasse [a]

[a] Institute for Simulation of reactive Thermo-Fluid Systems, TU Darmstadt, Otto-Berndt Str. 2, 64287 Darmstadt, Germany
[b] Institute for Reactive Flows and Diagnostics, TU Darmstadt, Otto-Berndt Str. 3, 64287 Darmstadt, Germany
[c] Engler-Bunte-Institute, Simulation of Reacting Thermo-Fluid Systems, Karlsruhe Institute for Technology, Engler-Bunte-Ring 7, 76131 Karlsruhe, Germany

ARTICLE INFO

Keywords:
Iron particle
Metal fuel
Single particle combustion
Iron nanoparticles
Resolved simulation

ABSTRACT

Iron powder is emerging as a promising carbon-free energy carrier that can be used for a clean iron-based energy cycle. The powder can be combusted with air to generate heat and power. Thereafter, the iron oxide powder is collected and regenerated by means of a thermochemical reduction with green H_2 closing the loop. During the combustion, the formation of nanoparticles poses challenges in terms of particulate emissions and material losses. Nanoparticles are difficult to separate from the exhaust gases and are respirable, which is why a comprehensive understanding of their formation and how to avoid them is necessary. In this study, a model for nanoparticle formation is introduced, which is based on the condensation of supersaturated iron/iron oxide vapor to liquid nanoparticles in the boundary layer of the burning iron microparticle. Resolved boundary layer simulations of single iron microparticles are compared with recent in situ measurements to investigate the onset of nanoparticle formation and characteristics of the nanoparticle cloud that is formed close to the burning parent microparticle. Nanoparticle formation and nanoparticle cloud evolution are investigated, considering combustion and transport processes in the boundary layer. It is shown that the particle temperature is the most important parameter for nanoparticle formation and a correct prediction of particle temperature evolution is crucial for nanoparticle prediction. Further analysis identifies convection and thermophoresis as the primary transport processes for the nanoparticle cloud, while diffusiophoresis is negligible. Additionally, the sensitivity of nanoparticle formation to the evaporation model and reaction mechanism is evaluated.

1. Introduction

Metal fuels are emerging as promising candidates for sustainable energy carriers due to their carbon-free oxidation, recyclability through chemical reduction, and high volumetric energy density [1]. Among other options, micron-sized iron powder has raised great interest since iron is widely available, cost-effective, and shows potential to retrofit existing coal infrastructure [2]. A key advantage of the concept of an iron-based energy cycle is that the powder burns in a heterogeneous manner according to early literature [3], allowing easy recovery of the combustion products for regeneration. Nevertheless, experimental findings revealed that a considerable amount of nanoparticles are among the combustion products [4–7]. Recent temporally and spatially resolved in situ optical measurements further demonstrate how nanoparticles are formed in the vicinity of micron-sized parent particles during combustion [8,9].

Nanoparticles are challenging to separate and collect from the exhaust gases [10], thus the efficiency of the recycling cycle could be impaired unless tailored capturing methods are developed. Besides, they also pose a health hazard as they are respirable [11]. Therefore, comprehensive knowledge of nanoparticle formation is crucial to the development of effective capturing methods or mitigation strategies.

Simulations of nanoparticle clouds can provide insights into the underlying physical mechanisms of nanoparticle formation and the characteristics of nanoparticles. Single particle simulations with a resolved boundary layer are an established method to investigate the combustion of coal and biomass particles [12–17], as well as metal fuels such as iron [18] and aluminum [19–21]. Thijs et al. [18] conducted resolved boundary layer simulations to study the nanoparticle release of iron particles, whereby the parent particle is interface resolved, and the nanoparticle phase is solved with an Eulerian approach. They investigated the effect of evaporation heat loss on the maximum temperature

* Corresponding author.
E-mail addresses: nguyen@stfs.tu-darmstadt.de (B.-D. Nguyen), scholtissek@stfs.tu-darmstadt.de (A. Scholtissek).

https://doi.org/10.1016/j.cej.2025.160039
Received 21 October 2024; Received in revised form 19 December 2024; Accepted 27 January 2025
Available online 4 February 2025

of the parent particle and analyzed the size distribution of the nanoparticles with a sectional population balance model. Since the formation of nanoparticles on a molecular level was still subject to great uncertainties, they assumed that nanoparticles consist of solid Fe_2O_3, which is formed from an infinitely fast conversion from FeO_2(g). FeO_2(g) in turn is formed by oxidation of gaseous iron molecules. In the research field of nanomaterial synthesis, iron oxide nanoparticles are produced from H_2/O_2-flames doped with $Fe(CO)_5$, where hydrogen plays a crucial role in the reaction mechanism from Fe(g) to Fe_2O_3 nanoparticles [22–24]. The mechanisms used for the synthesis of iron nanoparticles are also applicable to various configurations of iron microparticle combustion, particularly in environments where hydrogen-containing species are present in the surrounding atmosphere. In hot flows for example, where iron particles burn in the post-flame region of CH_4/O_2 flames [5,9], H_2O exist as a post-flame product. For laser-ignited particles in air [8], H_2O is present as a result of air humidity. However, recordings of nanoparticle clouds in the vicinity of combusting microparticles can also be found in a drop-tube furnace, where the ambient gas was presumably free from elemental hydrogen [25]. This observation indicates that there is at least another, yet insufficiently understood mechanism of nanoparticle formation that does not involve hydrogen-containing species.

The assumption of iron nanoparticles consisting of Fe_2O_3 is supported by X-ray diffraction measurements of nanoparticles collected at the exit of combustion devices [25–27]. However, the composition of the nanoparticles outside of a combustion device might differ from their composition in the vicinity of a combusting microparticle. Very recent molecular dynamics simulations by Li et al. [28] revealed that first, nanoparticles are formed by clustering of iron/iron oxide molecules due to attraction based on Coulomb forces, and second, the composition of nanoparticles at temperatures over 2000 K correspond to FeO. These new findings allow reformulation and further development of the modeling strategies for the formation of iron nanoparticles.

In our work, a model for nanoparticle formation is presented where supersaturated Fe(g) and FeO(g) vapor condensate into liquid nanodroplets. This is in line with the assumption for the nucleation of alumina nanodroplets [21]. The iron nanodroplets can further oxidize to the maximum oxidation state of FeO. In the remainder of this paper, nanodroplets are referred to as nanoparticles to be consistent with existing literature. Furthermore, for better readability, references to particles that are not specified as nanoparticles will imply the parent particle.

Using this model, the following open scientific questions are formulated:

Q1 Can current evaporation and nanoparticle models be utilized to capture the nanoparticle formation both qualitatively and quantitatively?
Q2 Which characteristics of single particle combustion are the most influential for nanoparticle formation?
Q3 What are the relevant transport processes to predict the evolution of nanoparticle clouds in the boundary layer of the parent microparticle?
Q4 How does the evaporation model affect the nanoparticle formation?
Q5 How do gas phase reactions affect the nanoparticle formation?

To this end, resolved simulations of single iron microparticles are conducted and compared with recent experimental measurements by Li et al. [28]. The paper is structured as follows. In Section 2, the experimental configuration by Li et al. [28] is briefly summarized. The numerical method is described in Section 3. In Section 4.1, the general processes during combustion are characterized. The numerical results are compared with experimental measurements in Sections 4.2 and 4.3 to address **Q1** and **Q2**. The research questions **Q3–Q5** are investigated in Section 4.4, 4.5, and 4.6.

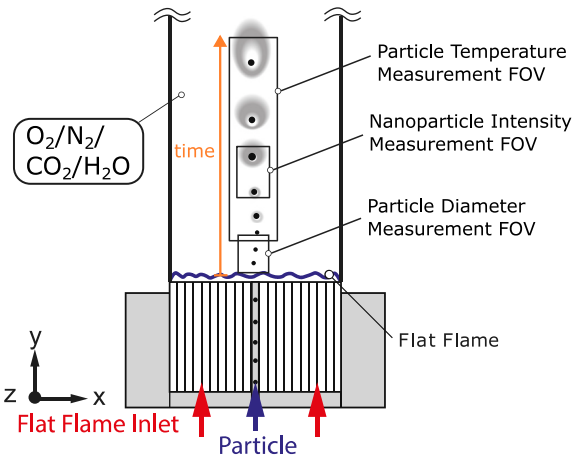

Fig. 1. Sketch of the experimental setup with measurement fields of view (FOV) [28].

2. Experimental configuration

The analysis of the present work utilizes experimental results from single iron particle combustion in hot laminar flows reported by Li et al. [28]. Previous works on the same combustion device have focused on the shape of the nanoparticle cloud [9], while recent work focuses on the parent particle temperature and the onset of nanoparticle formation [28]. The experimental configuration is briefly summarized below, with emphasis on the relevant aspects of this study. A detailed description of the experimental methods can be found in Li et al. [28].

Micron-sized iron particles are issued into a flat flame burner at atmospheric pressure. A premixed laminar flat methane flame, that is stabilized above the burner surface, provides a hot oxygen-enriched post-flame region such that particles are heated up and ignite. Due to excellent optical access, measurements can be conducted to provide well-defined boundary conditions and validation results. The measurements provide

- gas temperature via laser-induced fluorescence of OH radicals (prior to iron particle experiments) [29],
- particle temperature via two-color pyrometry [28],
- gas velocity via particle image velocimetry with inert tracers (prior to iron particle experiments) [29],
- particle velocity via particle tracking velocimetry with the iron particle itself as tracker [28],
- initial particle diameter via diffuse-backlight illumination (DBI) [28],
- nanoparticle intensity via DBI [28].

A sketch of the experimental setup with the respective fields of view (FOV) for the different measurements is shown in Fig. 1.

The species mole fractions of the post-flame gas have been determined from chemical equilibrium calculations using the species mixture of the GRI3.0 mechanism in Cantera [30]. The values are shown in Table 5. The measured initial particle diameters are binned into three groups $d_p = 40,\ 50,\ 60\,\mu m \pm 5\,\mu m$. The gas temperature, particle temperature, and the relative velocity between the particle and the gas are reported in Fig. 2.

The nanoparticle intensity, which is the attenuation of the background light, is measured in a 32×32px frame centered at the particle center location, where each pixel corresponds to a length of $5.17\,\mu m$. The intensity of each pixel is normalized by the background (i.e. unattenuated light) intensity. The nanoparticle intensity is calculated as the sum of the intensity of all pixels in the frame, excluding those occupied by the parent particle. The onset of the nanoparticle formation is defined as the time point t_{nano}, when the sum of the intensity of

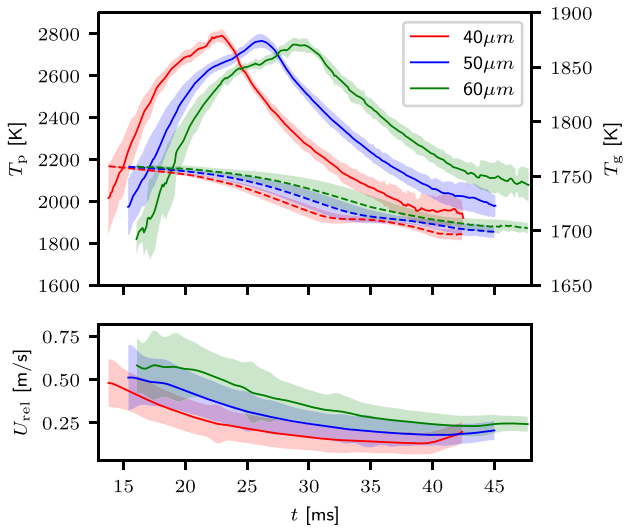

Fig. 2. Particle temperature T_p (solid lines), gas temperature T_g (dashed lines) along the burner center line, and relative velocity U_{rel} between the particle and the gas for the particle groups $d_p = 40,\ 50,\ 60\,\mu m \pm 5\,\mu m$.

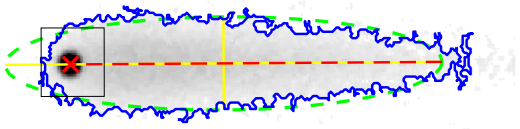

Fig. 3. Determination of the length of the nanoparticle cloud: The blue line indicates the boundary of the cloud, the green line is the fitted ellipse to the boundary, and the yellow lines are the minor and major axes of the ellipse. The red line depicts the distance between the particle center (red cross) and the farthest end of the major axis, which is defined as the length of the cloud. Determination of the nanoparticle intensity: The square depicts the frame, in which the nanoparticle intensity is measured.

all pixels exceeds a critical value of 1. T_{nano} is defined as the particle temperature at t_{nano}. The length of the nanoparticle cloud is measured by first detecting the cloud boundaries, then fitting an ellipse onto the shape, and lastly determining the distance between the particle center and the furthest point of the ellipse. A visual presentation of the measurement of the nanoparticle intensity and length of the nanoparticle cloud is shown in Fig. 3. It is worth mentioning that the nanoparticle intensity does not directly represent a physical quantity without additional calculations. These calculations, e.g. deriving a volume fraction from the intensity signal, require further information, such as the nanoparticle refractive index, a parameter that is not well-defined in the literature. Therefore, only the shape of the cloud and the onset of nanoparticle formation, not the intensity itself, are considered for comparisons with simulations.

3. Numerical configuration

3.1. Computational domain

For the resolved boundary layer simulations, a 2D axisymmetric domain is considered. A sketch of the computational domain is shown in Fig. 4a. The gas phase is fully resolved to capture heat and mass transfer. Similar to state-of-the-art 0D iron particle models [31–33], it is assumed that the heat and oxygen transfer inside the particle is infinitely fast. Thus, the solid phase is not resolved and instead represented by a 0D particle model, which interfaces with the fluid domain at the particle boundary. Preliminary mesh studies were performed and a hexahedral mesh containing 19752 cells was found to

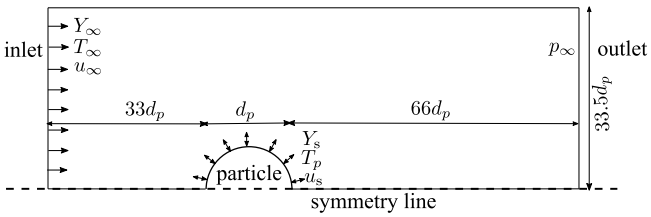

(a) Sketch of the computational domain. d_p is the particle diameter. Y, T, u, and p are the mass fraction, the temperature, velocity, and pressure, respectively. The subscript s denotes properties at the particle surface and the subscript ∞ denotes properties at the far field.

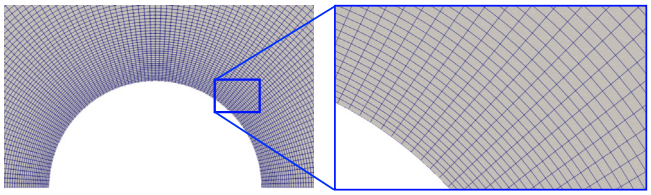

(b) Grid in the vicinity of the particle

Fig. 4. Computational domain.

be sufficient to capture transport phenomena in the boundary layer. Fig. 4b shows the grid in the vicinity of the particle. The grid spacing at the particle surface is $\Delta\theta/d_p = 0.029$ in the azimuthal direction and $\Delta r/d_p = 6.5 \times 10^{-3}$ in the radial direction.

3.2. Conservation equations

For the simulations, the open-source code OpenFOAM-v2012 is used as a basis and extended with iron-specific models. A two-phase solver is developed for the transport of nanoparticles in the condensed phase and the transport and reactions of gas molecules in the gas phase. Similar to other nanoparticle studies e.g. for alumina [21], it is assumed that the momentum transfer and the heat transfer are infinitely fast such that the condensed phase and the gas phase share the same convection velocity and temperature. The governing equations for mass, momentum, species, and enthalpy equations are

$$\frac{\partial(\alpha_g\rho_g)}{\partial t} + \frac{\partial(\alpha_g\rho_g u_i)}{\partial x_i} = -\alpha_g\dot{\omega}_c, \tag{1}$$

$$\frac{\partial(\alpha_c)}{\partial t} + \frac{\partial(\alpha_c u_i)}{\partial x_i} - \frac{\partial}{\partial x_i}\left(D_c\frac{\partial\alpha_c}{\partial x_i}\right) + \frac{\partial\left(\alpha_c V_{c,i}^T\right)}{\partial x_i} = \frac{\alpha_g\dot{\omega}_c}{\rho_c} \tag{2}$$

$$\frac{\partial(\alpha_g\rho_g u_i)}{\partial t} + \frac{\partial(\alpha_g\rho_g u_i u_i)}{\partial x_i} - \frac{\partial(\alpha_g\tau_g)}{\partial x_i} = -\alpha_g\frac{\partial p}{\partial x_i} - \alpha_g\dot{\omega}_c u_i, \tag{3}$$

$$\frac{\partial(\alpha_g\rho_g Y_k)}{\partial t} + \frac{\partial(\alpha_g\rho_g u_i Y_k)}{\partial x_i} + \frac{\partial\left(\alpha_g\rho_g Y_k V_{k,i}^D\right)}{\partial x_i} = \alpha_g\left(\dot{\omega}_{r,k} - \dot{\omega}_{c,k}\right) \tag{4}$$

$$\frac{\partial(\alpha_g\rho_g h)}{\partial t} + \frac{\partial(\alpha_g\rho_g u_i h)}{\partial x_i} + \frac{\partial(\alpha_g q_i)}{\partial x_i} = \alpha_g\frac{\partial p}{\partial t} + \alpha_g\dot{\omega}_{r,h} + \alpha_g\dot{\omega}_{c,h} - \frac{\partial}{\partial x_i}\left(h_c\alpha_c\rho_c V_{c,i}^T\right), \tag{5}$$

where the subscript g denotes the gas phase, the subscript c denotes the condensed nanoparticle phase, and the subscript r denotes the gas

phase reactions. α is the volume fraction, ρ is the density, u_i is the velocity vector, $\dot{\omega}_c$ is the mass transfer term between the gas phase and the condensed phase. D_c is the nanoparticle diffusion coefficient, which is set to zero throughout the paper, meaning that diffusiophoresis is not included, except for Section 4.4 where the effect of diffusiophoresis is investigated. $\rho_c = 4300\,\mathrm{kg\,m^{-3}}$ is the condensed phase density. $V_{c,i}^T$ is the thermophoretic velocity of the nanoparticles, given by [34]:

$$V_{c,i}^T = -0.55\frac{\nu_g}{T}\frac{\partial T}{\partial x_i}, \tag{6}$$

with ν_g as the kinematic viscosity. p denotes the pressure and τ_g is the viscous stress tensor given as

$$\tau_g = \mu_g\left(\nabla u_i + (\nabla u_i)^T - \frac{2}{3}I\nabla\cdot u_i\right). \tag{7}$$

$Y_k, V_{k,i}^D$ and $\dot{\omega}_{r,k}$ are the mass fraction, mixture averaged diffusion velocity, and net reaction rate of a species k, respectively. h denotes the sensible enthalpy, $\dot{\omega}_{r,h}$ denotes the net heat production rate from gas phase reactions, and $\dot{\omega}_{c,h}$ denotes the heat transfer term between the gas and the condensed phase. The transfer terms $\dot{\omega}_c$, $\dot{\omega}_{c,k}$ and $\dot{\omega}_{c,h}$ are described in Section 3.4.

q_i is the heat flux and consists of the convection and the radiation heat flux:

$$q_i = = q_{i,\mathrm{conv}} + q_{i,\mathrm{rad}}, \tag{8}$$

$$q_{i,\mathrm{conv}} = -\lambda_g\frac{\partial T}{\partial x_i} + \sum_k h_k\rho_g Y_k V_{k,i}^D, \tag{9}$$

$$q_{i,\mathrm{rad}} = \begin{cases}\epsilon\sigma T_p^4, & \text{particle surface}\\ 0, & \text{elsewhere}\end{cases} \tag{10}$$

where λ_g is the thermal conductivity, $c_{p,g}$ is the heat capacity, and h_k is the sensible enthalpy of a species k, $\epsilon = 0.7$ is the radiative emissivity [35], σ is the Stefan–Boltzmann constant, and T_p is the particle temperature.

The mixture-averaged diffusion velocity is given by

$$V_{k,i}^D = V_{k,i} - \sum_j Y_j V_{j,i} \tag{11}$$

with

$$V_{k,i} = -D_k\frac{1}{Y_k}\frac{\partial Y_k}{\partial x_i} - D_k\frac{1}{\bar{W}}\frac{\partial \bar{W}}{\partial x_i}, \tag{12}$$

where D_k is the mixture averaged diffusion coefficient and $\bar{W}$ is the mean molecular weight.

In the gas phase, the ideal gas law is applied and thermodynamic properties are calculated based on the NASA database [36].

3.3. Particle model

As mentioned in Section 3.1, the inner particle is assumed homogeneous. In this work, a model by Mi et al. [32] is used in the solid phase and a model by Mich et al. [33] is used in the liquid phase. The models are briefly summarized in Sections 3.3.1 and 3.3.2. In Section 3.3.3, the conditions at the particle–gas interface are described, which are in effect during both the solid and the liquid phases. For further details, the reader is referred to Refs. [32,33].

3.3.1. Solid phase oxidation

The solid-phase kinetic reaction rates are determined by assuming a multi-layer structure consisting of Fe(s), FeO(s) and Fe_3O_4(s):

$$\frac{\mathrm{d}m_i}{\mathrm{d}t} = \frac{4\pi r_i r_j}{r_i - r_j}\rho_i\, k_{\infty,i}\,\exp\left(-\frac{T_{a,i}}{T_p}\right), \tag{13}$$

where the subscript i refers to the oxides FeO(s) and Fe_3O_4(s), and the subscript j refers to the species with the next lower oxidation grade Fe(s) and FeO(s), respectively. r describes the outer radius of the respective phase. $k_{\infty,i}$ and $T_{a,i}$ are the kinetics parameters, which are the same as in Mi et al. [32]. The kinetic oxygen consumption rate is determined by

$$\frac{\mathrm{d}m_{O_2}}{\mathrm{d}t} = \frac{W_O}{W_{FeO}}\frac{\mathrm{d}m_{FeO}}{\mathrm{d}t} + \frac{4W_O}{W_{Fe_3O_4}}\frac{\mathrm{d}m_{Fe_3O_4}}{\mathrm{d}t}, \tag{14}$$

with W denoting the molecular weight. The oxygen consumption rate is limited by the maximum mass flux that occurs when the oxygen concentration at the particle surface is zero:

$$\dot{m}_{O_2,max} = A_p\rho_s D_{O_2,s}\left.\frac{\partial Y_{O_2}}{\partial r}\right|_{Y_{O_2,s}=0} \tag{15}$$

where the subscript s refers to the particle surface, and A_p is the particle surface area.

3.3.2. Liquid phase oxidation

In the liquid phase, it is assumed that the liquid phase is in thermodynamic equilibrium with the gas phase [33]. The vapor pressure of O_2 and Fe(g) is determined by equilibrium calculations performed with Thermo-Calc [37]. In the liquid burning phase, the partial pressures of O_2 and Fe(g) are therefore set at the particle surface. Thus, the evaporation of Fe(g) is initiated and the O_2 consumption is controlled by the surface concentration. The O_2 consumption mass flux and the Fe(g) evaporation mass flux is then determined by

$$\dot{m}_j = \dot{m}_{tot}Y_{j,s} - A_p\rho_s Y_{j,s}\left(V_{k,i}^D\cdot n_{i,s}\right), \tag{16}$$

where j denotes O_2 and Fe(g). $\dot{m}_{tot} = \dot{m}_{O_2} + \dot{m}_{Fe}$ is the total mass flux at the particle surface and $n_{i,s}$ denotes the surface normal vector at the particle surface.

The surface concentration of O_2 is tabulated as a function of the particle temperature and particle oxidation state. A distinct point exists at which the O_2 surface concentration rapidly increases from almost zero to the bulk concentration. This point is further referred to as the "oxidation limit". Before the oxidation limit, $Y_{O_2,s}$ is close to zero, thus Eq. (16) in combination with Eq. (12) collapses to Eq. (15). At the oxidation limit, which occurs at an oxidation degree between FeO and Fe_3O_4 [33], $Y_{O_2,s}$ rapidly increases, such that the O_2 consumption rate decreases.

Before that oxidation limit, the surface concentration of Fe(g) is mostly independent of the particle oxidation state. Therefore, the concentration is approximated with

$$X_{Fe,s} = 480973\exp(-41695/T_p). \tag{17}$$

Note that the above function yields the molar fraction, and needs to be converted to the mass fraction with $Y_{Fe,s} = X_{Fe,s}W_{Fe}/\bar{W}$ to be used with Eq. (16). The evaporation of species other than Fe(g) is not considered, since the vapor pressure of other species is at least one order of magnitude lower than the vapor pressure of Fe(g), as discussed in Li et al. [28]. After reaching the oxidation limit, the vapor pressure of the iron species drops to almost zero, hence evaporation is not considered after this point.

3.3.3. Conditions at the particle–gas interface

The temperature of the particle is determined from the total enthalpy calculated as

$$H_p = \sum_i^N m_i h_i(T_p), \tag{18}$$

where $N = \{\mathrm{Fe(s)},\ \mathrm{FeO(s)},\ \mathrm{Fe_3O_4(s)},\ \mathrm{Fe_yO_x(l)}\}$. The specific enthalpies are calculated with the NIST database [38]. The change in total enthalpy due to the incorporation of oxygen, the heat exchange with the gas phase, and the heat loss due to evaporation is calculated as

$$\frac{dH_p}{dt} = -A_p\left(q_{i,s}\cdot n_{i,s}\right) + \dot{m}_{O_2}h_{O_2} + \dot{m}_{Fe}h_{Fe}. \tag{19}$$

The particle volume is subject to a continuous change due to the mass change resulting from oxidation and evaporation, and due to

temperature and oxidation state dependent density change:

$$V_p = \sum_i^N \frac{m_i}{\rho_i}. \tag{20}$$

A dynamic mesh is used to account for the growth of the particle diameter. The densities are taken from Refs. [39–42].

The Stefan flow is a convection flux resulting from the production or removal of species at an interface. It is proportional to the total mass flux $\dot{m}_{tot}$ over the particle surface. The Stefan flow velocity at the particle boundary is given as:

$$u_{i,s} = n_{i,s} \frac{\dot{m}_{tot}}{A_p \rho_s}. \tag{21}$$

3.4. Nanoparticle formation

The formation mechanism of iron/iron oxide nanoparticles is still subject of ongoing research. There are only a few in situ measurements of nanoparticle formation [8,9,28] and until recently, the composition of nanoparticles has been examined ex situ only. In such ex situ examinations, the composition of nanoparticles is found to be predominantly Fe_2O_3 [25–27]. However, there are indications that the nanoparticles do not necessarily consist of Fe_2O_3 when they are initially formed. First, according to the Fe/O phase diagram, Fe_2O_3 is stable only at temperatures below 1700 K, which has also been pointed out by other authors [28,33,43,44]. Well established mechanisms for iron nanoparticle synthesis in hydrogen flames were developed for temperatures under 1600 K [22–24], where Fe_2O_3 is likely the initial composition of nanoparticles. In the case of iron microparticle combustion, it should be considered that in situ measurements [8, 9,28] have shown that nanoparticles are formed close to the parent particle, where temperatures are well above 2000 K during diffusion-limited combustion. Therefore, mechanisms that were developed for nanoparticle synthesis [22–24] might not be applicable in this case.

Second, recent molecular dynamics simulations suggest that the composition of nanoparticles is likely FeO at temperatures around 2000 K [28]. Therefore, we hypothesize that nanoparticles initially consist of (liquid) FeO, which is formed by condensation of gaseous iron/iron oxide. This hypothesis is shared by Wiinikka et al. [26] who performed Transmission Electron Microscopy analysis on iron nanoparticles. Considering modeling approaches for other metal fuels, this assumption is consistent with the model for alumina nanoparticles by Finke and Sewerin, who investigated aluminum combustion in a homogeneous reactor [45] and the gas phase processes in the vicinity of an oxidizing aluminum particle [21].

For the present model, it is assumed that condensation mostly occurs at the surface of the nanoparticles. Therefore, the collision rate of gaseous molecules onto the nanoparticles determines the condensation rate:

$$\dot{\omega}_{c,k} = Z_{c,k} = \gamma m_k n_k n_c (\sigma_k + d_c)^2 \sqrt{\frac{\pi k_B T}{2 m_k}}, \tag{22}$$

$$m_k = \frac{W_k}{N_A}, \quad n_k = \frac{X_k p}{k_B T}, \quad n_c = \frac{6\alpha_c}{\pi d_c^3}, \tag{23}$$

where k refers to Fe(g) and FeO(g) since these are the only species that are stable in both the gas and the liquid phase. γ is the sticking coefficient, m is the mass of one molecule, n is the molecule or particle number density, σ is the molecule diameter, d_c is the diameter of the nanoparticles, k_B is the Boltzmann constant, and N_A is the Avogadro number.

Prior to the formation of any nanoparticles, Eq. (22) equals zero preventing the initiation of nanoparticle formation and further condensation. Therefore, the collision rate of Fe molecules onto each other is used as the condensation rate below a threshold of $\alpha_c = 1 \times 10^{-5}$:

$$\dot{\omega}_{c,Fe} = Z_{Fe} = \gamma 2 m_{Fe} n_{Fe}^2 \sigma_{Fe}^2 \sqrt{\frac{\pi k_B T}{m_{Fe}}}. \tag{24}$$

Table 1
Rate coefficients for the gas phase reactions [46] (units: cm, s, mol, K). $k = AT^n \exp -E_a/(R_u T)$.

Reaction	A	n	E_a/R_u
$Fe(g) + O_2 \rightleftharpoons FeO(g) + O$	3.1×10^{15}	0	13 200
$FeO(g) + O_2 \rightleftharpoons FeO_2(g) + O$	1.7×10^{14}	0	9300

Regardless of how fast condensation occurs, the condensation process is governed by the supersaturation of iron and iron oxide vapor. Therefore, it is ensured that the amount of condensed mass does not exceed the amount of supersaturated vapor. The maximum condensation rate is

$$\dot{\omega}_{c,k} \leq \frac{\rho_g (Y_k - Y_{k,v})}{\Delta t}, \tag{25}$$

where Y_k is the mass fraction of Fe(g) and FeO(g) that exist due to evaporation and gas phase reaction and Δt is the current time step. $Y_{k,v}$ is the mass fraction that can exist as vapor, which is calculated from the vapor pressure:

$$\frac{p_{Fe,v}}{p} = 480973 \exp(-41695/T_p), \tag{26}$$

$$\frac{p_{FeO,v}}{p} = 679076 \exp(-51570/T_p). \tag{27}$$

Note that Eq. (26) is consistent with Eq. (17), which is used to initiate evaporation of Fe(g) from the parent particle. Therefore, condensation of Fe(g) occurs when Fe vapor is transported away from the particle, where the rapidly decreasing temperature leads to a significant drop of the vapor pressure (compared with the particle surface conditions), causing supersaturation. Although the present model does not consider the evaporation of FeO(g) from the parent particle, FeO(g) can be formed by gas phase reactions, hence the condensation of FeO(g) is considered. The gas phase reactions are adapted from Giesen et al. [46] (c.f. Table 1).

The condensation heat release is given by

$$\dot{\omega}_{c,h,k} = \dot{\omega}_{c,k} h_{vap,k}, \tag{28}$$

where $h_{vap,k}$ denotes the heat of vaporization.

Oxidation of the nanoparticles is enabled by assuming that the oxidation rate is the same as the collision rate of O_2 molecules with nanoparticles, such that $\dot{\omega}_{c,O_2} = Z_{c,O_2}$, whereby the maximum oxidation state is FeO. Note that further oxidation to Fe_2O_3 is not considered in this study since the ambient temperature remains above 1700 K in the relevant region of interest (cf. Fig. 2), a temperature range for which Fe_2O_3 is thermodynamically unstable [33,43]. For future works, the model can be extended to include further oxidation to Fe_2O_3.

The oxidation heat release is given by

$$\dot{\omega}_{c,h,O_2} = \dot{\omega}_{c,O_2} h_{comb}, \tag{29}$$

with h_{comb} being the combustion enthalpy.

The total transfer term between the gas and the condensed phase is given by summing the condensation terms and oxidation terms:

$$\dot{\omega}_c = \dot{\omega}_{c,Fe} + \dot{\omega}_{c,FeO} + \dot{\omega}_{c,O_2}, \tag{30}$$

$$\dot{\omega}_{c,h} = \dot{\omega}_{c,h,Fe} + \dot{\omega}_{c,h,FeO} + \dot{\omega}_{c,h,O_2}. \tag{31}$$

The values for the condensation model are given in Table 2. For all collision rates, we assume a sticking coefficient of $\gamma = 0.5$. A preliminary study with sticking coefficients between 0.5 and 1 showed that the results are insensitive to the sticking coefficients. The diameter of the nanoparticles is set to $d_c = 45$ nm and held constant. This value has been evaluated from Scanning Electron Microscope (SEM) images of combusted particles [49]. Preliminary studies showed that the nanoparticle formation is insensitive to the diameter in Eq. (22) (variation between 5–60 nm). Regardless of that, small nanoparticles under 10 nm can experience diffusiophoresis since their size is in the

Table 2
Condensation model properties: molecule diameter σ, nanoparticle diameter d_c, nanoparticle mass density ρ_c, evaporation enthalpy h_{vap}, combustion enthalpy h_{comb}.

Property	Value	Reference
σ_{Fe}	4.3 Å	[47]
σ_{FeO}	4.3 Å	[47]
σ_{O_2}	3.55 Å	[48]
d_c	45 nm	[49]
ρ_c	4300 kg m^{-3}	[42]
$h_{vap,Fe}$	6.267×10^6 J kg^{-1}	[38]
$h_{vap,FeO}$	5.651×10^6 J kg^{-1}	[38]
h_{comb}	4.844×10^6 J kg^{-1}	[50]

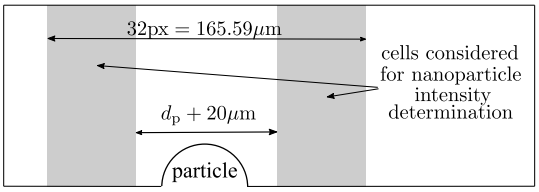

Fig. 5. Sketch of the domain (gray), where the condensed phase volume fraction is integrated, to compare with experimental nanoparticle intensity.

range of gas molecules [51], which could have an impact on the characteristics of the nanoparticle cloud. This is discussed in more detail in Section 4.4. A model accounting for the evolution of the size distribution of nanoparticles is out of scope for the present study and remains a subject for future research.

3.5. Determination of nanoparticle quantities

The experimental determination of nanoparticle formation onset is based on the nanoparticle intensity. The attenuation of background light, represented by the nanoparticle intensity, is directly influenced by the amount of nanoparticles. Therefore, the integrated nanoparticle volume fraction is used as a similar means to determine the onset of nanoparticle formation in the simulation. A sketch of the integration domain is shown in Fig. 5. In the streamline direction, the same frame length as in the experiment of 32px is applied. Perpendicular to the streamline direction, the whole height of the domain is used for integration since the DBI measurement records a line-of-sight integrated signal. Consistent with the experimental procedure, a gap of $d_p + 20\,\mu$m at the parent particle is left out since nanoparticles that are close to, or above the parent particle cannot be distinguished from the parent particle. This corresponds to a gap of around 2px on each side of the parent particle. Additionally, the gap accounts for the growth of the particle diameter during combustion. A sensitivity analysis showed that, although the absolute integrated value differs with the size of the gap, the normalized value and the evolution of the normalized value do not change.

The experimental definition for the determination of the nanoparticle formation onset is not applicable in the simulation case (cf. Section 2). Instead, the time of onset t_{nano} is defined as the point of maximum curvature in the integrated α_c evolution. For the measurement of the nanoparticle cloud length, the same method is used.

3.6. The Hertz–Knudsen–Schrage evaporation model

In Section 3.3.2, an evaporation model is introduced that assumes saturation at the particle surface, and thus, the partial pressure of Fe(g) at the surface is the same as the vapor pressure. This model has been used for iron particle simulations [18,33,43] and for earlier aluminum particle simulations [19,52,53]. However, more recent models for aluminum particles used the Hertz–Knudsen relation [54,55] with the Schrage correction [56], further referred to as Hertz–Knudsen–Schrage (HKS) relation, to model evaporation [20,21,45,57]. The HKS relation considers the net evaporation mass flux to be a balance between evaporation of molecules from a surface and condensation of molecules on the same surface, derived from gas kinetic theory:

$$\dot{m}_k = \frac{2\psi}{2-\psi}\sqrt{\frac{W_k}{2\pi R_u}}\left(\frac{p_v(T_{liq})}{\sqrt{T_{liq}}} - \frac{p_{i,s}}{\sqrt{T_s}}\right), \tag{32}$$

where ψ is the sticking coefficient between the evaporated/condensed molecules and the surface, p_v is the saturated vapor pressure, T_{liq} is the temperature of the liquid phase, $p_{i,s}$ is the partial pressure of the evaporated/condensed species at the surface, and T_s is the temperature of the gas phase at the surface. Applying the HKS relation to the evaporation of Fe(g), the net evaporation mass flux reads:

$$\dot{m}_{Fe} = \frac{2\psi}{2-\psi}\sqrt{\frac{W_{Fe}}{2\pi R_u T_p}}\left(p_{Fe,v}(T_p) - p_{Fe,s}\right), \tag{33}$$

with $$p_{Fe,s} = pY_{Fe,s}\bar{W}/W_{Fe}, \tag{34}$$

where $T_{liq} = T_s = T_p$ is assumed. $p_{Fe,v}(T_p)$ is obtained with Eq. (26). The main difference to the saturation evaporation model in Section 3.3.2 is that the evaporation mass flux is enforced with Eq. (33) and $p_{Fe,s}$ is computed in the HKS relation. In contrast, in the saturation evaporation model, $p_{Fe,s} = p_{Fe,v}(T_p)$ is enforced while the evaporation mass flux is a solution of Eq. (16).

The sticking coefficient ψ for Fe(g) molecules with an Fe_xO_x(l) surface is unknown. Aluminum particle simulations usually assume unity sticking coefficient [20,21,57]. In Section 4.5, the two above described evaporation models are compared, and the sensitivity to the sticking coefficient is investigated.

3.7. Reaction-driven nanoparticle formation model

Since the nanoparticle formation model in this study is fundamentally different from the first study of iron nanoparticles during the combustion of microparticles by Thijs et al. [18], a qualitative comparison of both models is drawn in Section 4.6. In the study by Thijs et al. [18], Fe_2O_3(s) are considered as nanoparticles. They are formed by infinitely fast conversion from FeO_2(g), which in turn is formed by oxidation of Fe(g) and FeO(g). Thus, the main difference to the model in the present study is that the formation rate of nanoparticles is limited by the production rate of FeO_2(g). Heat release from the conversion to Fe_2O_3(s) is considered, while condensation heat release does not exist, which is another difference to this study. The reaction mechanism that was used in Thijs et al. [18] is adapted from Nanjaiah et al. [23], and it is given in Table 3. Notably, the first and second reactions are similar to the reaction mechanism adapted from Giesen et al. [46] (Table 1), while reaction $Fe(g) + O_2 + M \rightleftharpoons FeO_2(g) + M$ is only included in the reaction mechanism by Nanjaiah et al. [23]. Giesen et al. [46] experimentally investigated the latter reaction and concluded that it is only dominant for temperatures under 1650 K, while reactions $Fe(g) + O_2 \rightleftharpoons FeO + O$ and $FeO(g) + O_2 \rightleftharpoons FeO_2(g) + O$ are dominant for temperatures above 1650 K. This explains our choice of the mechanism in Table 1.

However, the temperatures in the boundary layer usually exceed 2500 K, where reaction mechanisms are yet unexplored and uncertainties persist. To this end, the sensitivity of nanoparticle formation to the reaction mechanism is analyzed in Section 4.6.

3.8. Simulation cases

Twelve boundary layer resolved simulations of oxidizing iron particles with nanoparticle formation are carried out in this study which are further discussed in Section 4. Modeling details are listed in Table 4 and the case number will be used throughout the paper to refer to the specific cases. Other boundary conditions remain consistent for all cases (c.f Table 5).

Table 3
Rate coefficients for the gas phase reactions considered in [18], based on [23] (units: cm, s, mol, K). $k = AT^n \exp -E_a/(R_u T)$.

Reaction	A	n	E_a/R_u
$Fe(g) + O_2 \rightleftharpoons FeO + O$	3.1×10^{15}	0	11 225
$FeO(g) + O_2 \rightleftharpoons FeO_2(g) + O$	3.1×10^{10}	0.4	8200
$Fe(g) + O_2 + M \rightleftharpoons FeO_2(g) + M$	1.2×10^{18}	0	554
$2O + M \rightleftharpoons O_2 + M$	1.2×10^{17}	−1	0

4. Results and discussion

First, the physical mechanisms during combustion of a single iron particle are discussed in Section 4.1. In Sections 4.2 and 4.3, the simulation results are compared with experimental measurements of the nanoparticle formation onset. The effect of thermophoresis and diffusiophoresis on the nanoparticle cloud are analyzed in Section 4.4, using experimental measurements of the nanoparticle cloud. The effect of the evaporation model is discussed in Section 4.5. Lastly, the sensitivity of nanoparticle formation to reaction mechanisms is evaluated in Section 4.6.

4.1. Mechanisms during combustion of a single iron microparticle

In this Section, the main physical mechanisms during combustion, as predicted by the current particle model, are shown for Case 1. Fig. 6a shows the particle temperature, heat release rate from chemical conversion, and heat loss due to convection, radiation, and evaporation. Complementary, Fig. 6b shows the oxygen consumption rate, the evaporation rate, the Stefan flow velocity, and the nanoparticle volume fraction. During initial oxidation, the heat release is significantly higher than the heat loss, leading to a thermal runaway. The evaporation rate is still negligible at this point. At around $t = 12$ ms, the particle starts to release gaseous Fe. The evaporation mass flux increases further and even surpasses the oxygen consumption mass flux. Therefore, the Stefan flow changes its orientation from being directed towards the particle to pointing outwards. This further enhances the evaporation and slows down the oxygen consumption. Note that the Stefan flow does not always change its direction during particle combustion. In this particular case, high ambient temperatures lead to increased particle temperatures and cause the evaporation mass flux to exceed the oxygen mass flux. For cases with low ambient temperatures, e.g. laser-ignited particles in air [7], or low oxygen concentrations, the evaporation rates are usually low [18,43] and therefore, the Stefan flow points towards the particle during the entire combustion phase.

Due to high evaporation rates, the evaporation heat loss is the most dominant heat transfer term in this case. At around $t = 19$ ms, there is a temporary plateau in the temperature, since the heat loss has increased to the point where it is equal to the heat release. At the stoichiometric ratio of FeO, where further oxidation to Fe_3O_4 starts, there is a jump in the sensible enthalpy according to thermodynamic equilibrium calculation. Therefore, the temperature rises again. After a short time, the particle reaches its oxidation limit and the oxygen consumption rate together with the heat release rate reduces tremendously. This causes the particle temperature to decrease since the heat release cannot compensate for the heat loss. This process is referred to as “reactive cooling” and has been explained in more detail in Mich et al. [33]. During the reactive cooling, the vapor pressure of Fe is negligible and thus, any further relevant evaporation does not happen.

The evolution of the normalized integrated nanoparticle volume is an indicator of the nanoparticle formation, since the volume is only integrated in a small region around the particle. It does not account for the entire nanoparticle cloud. The evolution can be categorized into three phases:

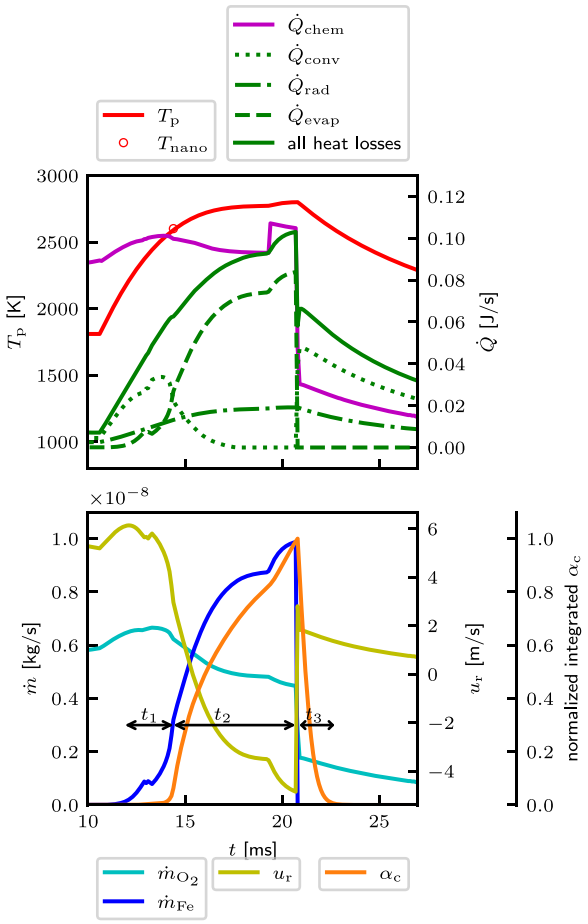

Fig. 6. Particle temperature T_p, heat transfer rates $\dot{Q}$ and mass transfer rates $\dot{m}$ between the particle and the gas phase, Stefan flow velocity u_r, and normalized integrated volume fraction of the nanoparticles α_c during particle combustion for a particle with $d_p = 40\,\mu$m.

t_1 - Onset of nanoparticle formation: The evaporation of Fe starts. At the same time, nanoparticles start to form. However, the amount is still small and they are too close to the surface to be detected.

t_2 - Formation of nanoparticle cloud: There are enough nanoparticles to be detected and to form a cloud. The beginning of this phase is dependent on the experimental detection method [28].

t_3 - Nanoparticle cloud tear-off: The evaporation and thus nanoparticle formation stops. The nanoparticles that have been formed are transported away from the particle.

Fig. 7 shows the nanoparticle cloud during the three phases. In the first phase, only a slight amount of nanoparticles is located in the vicinity of the particle. In the second phase, a visible cloud has formed. Since diffusiophoresis is not considered, the nanoparticles are transported downstream via convection only, which causes the length of the cloud to grow. It is evident that the length of the cloud is sensitive to the relative velocity between the particle and the gas phase, and that the final length is sensitive to the duration of nanoparticle formation. In the third phase, the nanoparticle formation stops. The nanoparticles in the vicinity of the parent particle are transported along the radial direction away from the parent particle due to thermophoresis and further away in downstream direction due to convection. This aspect is discussed in more detail in Section 4.4.

Fig. 8 shows a plot of quantities in the boundary layer along a line from the particle surface in radial direction. The line is depicted as an arrow in Fig. 7 at $t = 20$ ms, corresponding to the time point at which the sample data was obtained. During the evolution of the

Table 4
The 12 simulation cases considered in this study. "sat." denotes the evaporation model described in Section 3.3.2, which assumes vapor saturation at the particle surface, "C" represents the condensation-driven model that is described in Section 3.4 and "R" the reaction-driven model by Thijs et al. [18].

Case	1	2	3	4	5	6	7	8	9	10	11	12
d_p [μm]	40	50	60	40	50	60	40	40	40	40	40	40
T_p	Eq. (18)	Eq. (18)	Eq. (18)	Fig. 2	Fig. 2	Fig. 2	Fig. 2	Fig. 2	Fig. 2	Fig. 2	Fig. 2	Fig. 2
Thermophoresis	yes	yes	yes	yes	yes	yes	no	yes	yes	yes	yes	yes
Diffusiophoresis	no	no	no	no	no	no	no	yes	no	no	no	no
Evaporation	sat.	sat.	sat.	sat.	sat.	sat.	sat.	sat.	HKS	sat.	sat.	sat.
Reaction mechanism	Table 1	Table 1	Table 1	Table 1	Table 1	Table 1	Table 1	Table 1	Table 1	Table 3	Table 1	Table 3
Nanoparticle formation	C	C	C	C	C	C	C	C	C	C	R	R

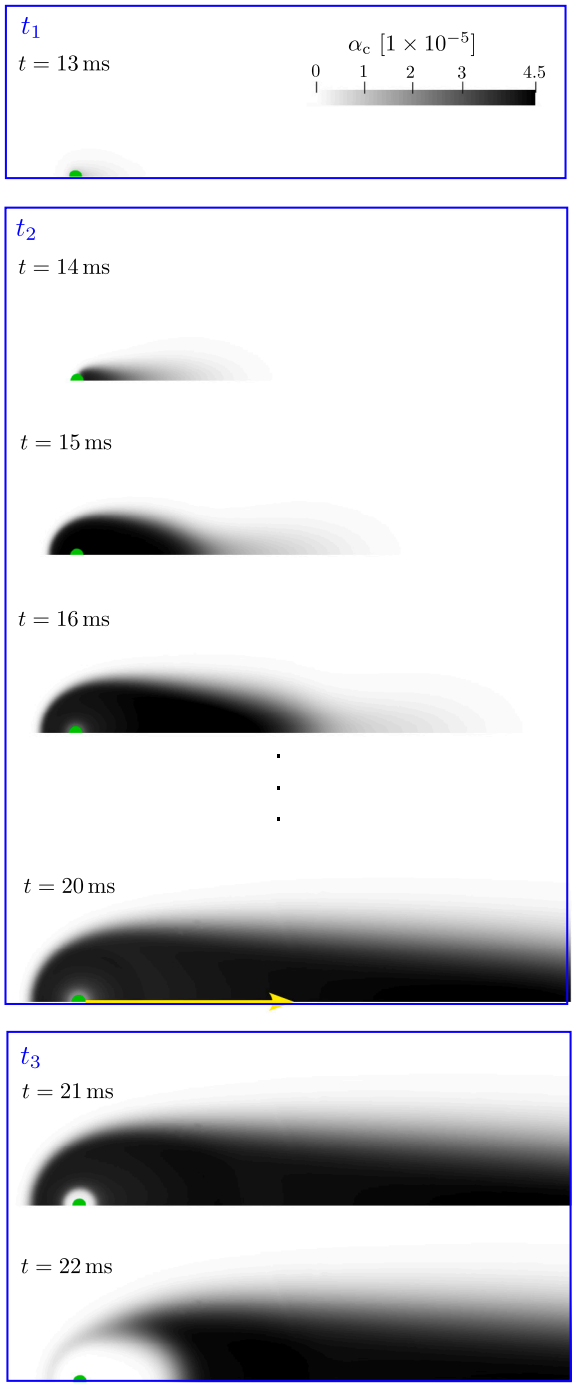

Fig. 7. Distribution of the nanoparticle volume fraction during different phases. The parent particle ($d_p = 40\,\mu m$) is depicted in green.

Table 5
Boundary conditions applied to all simulation cases.

Boundary condition	Value
X_{O_2}	0.2
X_{N_2}	0.596
X_{CO_2}	0.068
X_{H_2O}	0.135
T_∞	1750 K
$T_{p,0}$	300 K
u_∞	exp. profile (see Fig. 2)
p_∞	1 atm

particle, the absolute values of the quantities shown change but the characteristics remain the same most of the time. Fig. 8a shows the condensation rate of Fe and FeO molecules. In combination, they represent the nanoparticle formation rate. Nanoparticles are formed very close to the surface, most of them within the first 50 μm from the particle surface. It is obvious that the condensation rate of Fe is around three times higher than the condensation rate of FeO. Since the heat of vaporization of Fe and FeO are similar to each other (cf. Table 2), the heat release due to condensation maintains the proportion, shown in Fig. 8b. Fig. 8b also shows the heat release due to nanoparticle oxidation and gas phase reactions. Most of the nanoparticle oxidation occurs close to the particle surface as well. When the oxidation rate is zero, which happens at around 50 μm from the particle surface, the nanoparticles have reached their maximum oxidation state of FeO. The local minimum in the Fe condensation rate comes from the fact that oxidation heat release has its maximum here, which shifts the temperature dependent vapor pressure of Fe. Gas reactions generate a heat sink due to the endothermic reaction $FeO(g) + O_2 \rightleftharpoons FeO_2(g) + O$, which is dominant in this case. Overall, the total heat is positive. Despite this, the location with the highest temperature remains at the particle surface, since the particle temperature keeps rising up until the peak. Unlike aluminum particle combustion [21], where the gas temperature exceeds the particle temperature, the condensation heat release in iron particle combustion is not a dominant effect. Fig. 8a further shows the convection and thermophoresis velocities. Thermophoresis drives the nanoparticles from hot regions to cold regions. At this particular time point, the Stefan flow is also directed away from the particle due to strong evaporation. Both transport mechanisms drive the nanoparticles from their formation location away from the parent particle.

4.2. Particle temperature and the onset of nanoparticle formation

In Fig. 9, the computed particle temperature evolution is compared with the experimental particle temperature for cases 1 to 3. Furthermore, the onset of nanoparticle formation t_{nano} is marked as a vertical line. The particle temperature at the onset T_{nano} is marked on the temperature curve. The corresponding integrated nanoparticle volume fraction is shown for each case. In all cases, the peak temperature shows a good agreement and the cooling slope is accurately predicted. The numerical heating slope shows deviations from the experimental measurements in the case with $d_p = 40\,\mu m$. In the cases with $d_p = 50\,\mu m$ and 60 μm, the deviations in the heating slope are more significant and

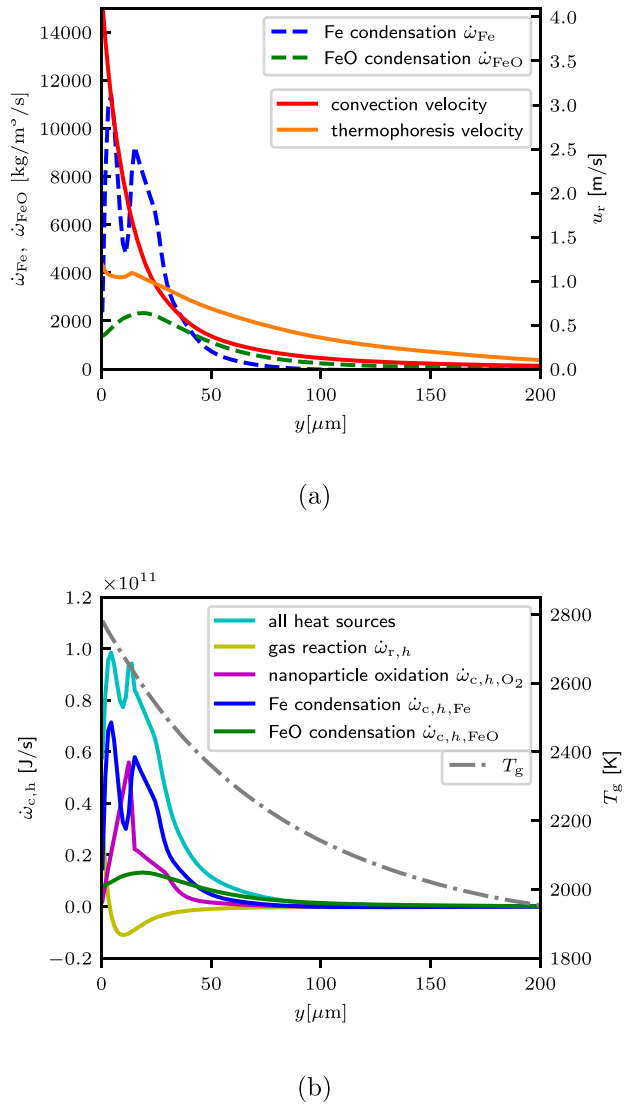

Fig. 8. (a) Condensation rates, convection and thermophoresis velocities, (b) heat sources/sinks, and the gas temperature along a line from the particle surface in radial direction for a particle with $d_p = 40\,\mu m$.

increase with larger diameter. It can be observed that the numerical T_{nano} agrees well with the experimental value in all cases. Despite that, the onset of nanoparticle formation is predicted too early in the simulations due to the deviations during particle heating. One possible reason for the deviations is that larger particles could be more affected by internal transport resistance [58]. This highlights the sensitivity of the nanoparticle formation on the particle temperature, which is an answer to **Q2**, since even a small deviation as in $d_p = 40\,\mu m$ can cause a non-negligible deviation in t_{nano}. This indicates that, for the investigation of nanoparticle formation, it is crucial to accurately predict the complete temperature evolution, rather than just the peak temperature and the time to peak.

The DBI measurements of the nanoparticle intensity were not obtained for the entire heating phase, hence the termination of nanoparticle formation is not recorded for the shown cases. However, in other experiments [8,9,59], it was shown that nanoparticle formation terminates at t_{peak}, which agrees with the simulations. Therefore, it can be concluded that the termination of nanoparticle formation is correctly predicted, while the onset requires further consideration.

4.3. Nanoparticle formation with imposed particle temperature

In order to separate uncertainties associated with the temperature increase of the particle from nanoparticle formation, the particle temperature evolution measured in the experiment is imposed on the particle. Instead of computing the particle temperature from the enthalpy balance equation, the experimental particle temperature is set as a Dirichlet boundary condition during particle heating. By this approach, the evaporation time scales and conditions in the particle boundary layer reflect the experiments more accurately. The Stefan flow, the O_2 consumption rate and the evaporation rate are still calculated according to the particle model (Eq. (16)), since a qualitatively correct Stefan flow is still important for the flow characteristics. The particle mass and density are kept constant during particle heating since the influence of the particle diameter on the nanoparticle formation is negligible. During particle cooling, Section 4.2 shows that the temperature is correctly predicted by the particle model. Therefore, the temperature is again computed from the enthalpy equation (Eq. (5)) during the cooling phase. The model is initialized with the mass and density corresponding to the temperature peak computed in the previous simulation phase. The cases shown in this Section correspond to cases 4 to 6 in Table 4.

Fig. 10 shows the particle temperature and integrated nanoparticle volume fraction with the imposed experimental temperature during the heating phase. It is observed that the onset of nanoparticle formation is now accurately predicted. The temperature T_{nano} and time t_{nano}, at which nanoparticles are first detected, are only slightly underpredicted in the simulations. In Fig. 11, T_{nano} is depicted in relation to the diameter. The difference between T_{nano} predicted in the simulations and the experimentally determined T_{nano} is 24 K at most, with the numerical values for $d_p = 40\,\mu m$ and $60\,\mu m$ being at the lower limit of the standard deviation. Furthermore, the weakly linear trend related to the particle diameter is accurately predicted. Therefore, a first answer can be given to question **Q1**: The particle temperature, at which nanoparticles start forming, can be quantitatively captured. The termination of nanoparticle formation is correctly predicted at the peak temperature. However, the particle model cannot quantitatively reproduce the temperature evolution during the particle heating phase. Without the accurate particle temperature, the onset of nanoparticle formation can only be predicted qualitatively. Regarding the amount of formed nanoparticles, the experimental data does not allow to draw a quantitative comparison. The latter is therefore the subject of future research.

While the integrated nanoparticle volume in a small region around the parent particle is an indicator of nanoparticle formation, it is important for the development of collecting methods to evaluate the total volume of nanoparticles. Fig. 12 shows the integrated nanoparticle volume over the entire domain and the formation rate. It can be observed that the formation rate increases with progressing time. This can be explained by the fact that the vapor pressure solely depends on the temperature (Eq. (17)), and thus the amount of condensing molecules depends on the difference between the parent particle temperature and the bulk gas temperature, whereby the particle temperature steadily rises but the bulk gas temperature remains constant. The formation rate is independent of particle diameter. This can be explained by the fact that there are two counteracting effects on the evaporation rate. At the same particle temperature, smaller particles release less vapor due to their smaller surface area. However, the particle heating rate is proportional to $1/d_p^2$ [60], which in turn enhances the evaporation rate for smaller particles. The drop in the formation rate coincides with t_{peak} and the termination of evaporation. However, the formation rate shown in Fig. 12 remains still slightly above zero for a certain time. This can be explained by the fact that first, the particle temperature decreases and thus the temperature in the boundary layer decreases, and second, the vapor is transported into colder regions. This results in additional

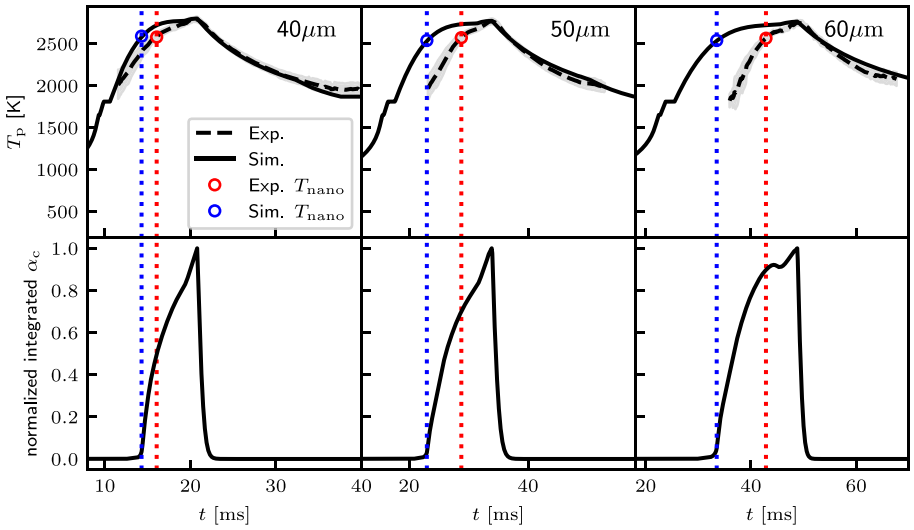

Fig. 9. Top: Numerical and experimental particle temperature evolution. Bottom: Numerically obtained volume of nanoparticles. Vertical lines depict the onset of nanoparticle formation and markers on the temperature curves indicate the temperature T_{nano}, at which the onset occurs. All curves are aligned at the temperature peak.

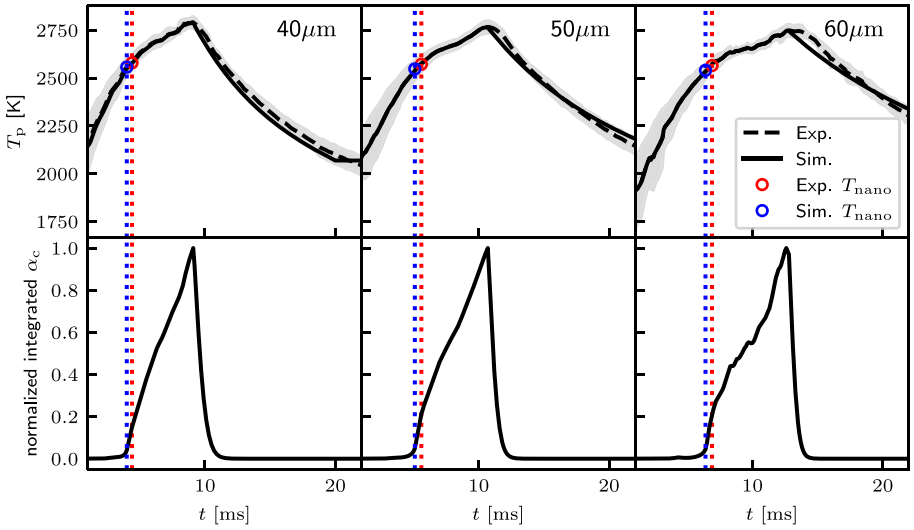

Fig. 10. Top: Numerical and experimental particle temperature evolution with the experimental particle temperature set as boundary condition during the heating phase. Bottom: Numerically obtained volume of nanoparticles. Vertical lines depict the onset of nanoparticle formation and markers on the temperature curves indicate the temperature, at which the onset occurs. All curves are aligned at the temperature peak.

nanoparticle formation due to condensation farther away from the parent particle. In general, the total volume of nanoparticles increases with increasing particle diameter, mainly due to a longer particle heating time. The trend of the total nanoparticle volume is similar to the trend shown in Cen et al. [59]. The fast-rising trend before termination and the slow-rising trend after termination of evaporation can also be found in their measurements. Cen et al. [59] also found that, right before termination, the total volume shows a linear trend, which corresponds to a constant formation rate, and argued that the trend should be significantly larger due to the increase in vapor pressure. Although a constant formation rate cannot be found in the current study, the formation rate can be influenced by multiple factors, e.g. the ambient temperature, the slip velocity, and the oxygen concentration, which in turn affects the Stefan flow. Thus, a linear trend might also be possible depending on the operating conditions. Additionally, Cen et al. [59] observed that the formation rate increases with decreasing ambient temperature, which might be due to the fact that lower ambient temperature results in lower vapor pressure. Nevertheless, it does not imply that increasing the ambient temperature would suppress nanoparticle formation, since the vapor would condense as soon as it enters a colder region of the combustion system. This highlights the difficulty in comparing numerical results to ex situ measurements. Upon integrating the evaporation mass flux over time, it is found that the mass loss with respect to the initial mass amounts to 12%, 8%, and 6% for d_p = 40 µm, 50 µm and 60 µm, respectively. Although these values should be taken with prudence, since the mechanisms during particle heating are not yet conclusive, they are comparable to those documented in the literature. Wiinikka et al. [26] reported that nanoparticles constitute up to 4% of the combustion products of 60 µm-sized iron particles burning in air at 1473 K. Poletaev and Khlebnikova [61] observed 10%–20% of nanoparticles among the combustion products of 5 µm-sized iron particles in ambient conditions of $X_{O_2} = 0.2 - 0.4$. Estimation of the nanoparticle volume via in situ light-extinction-measurements by Cen et al. [59] indicates that 2%–4% of the initial mass is converted into nanoparticles, with boundary conditions of $d_p = 20 - 40$ µm, $T_g = 1400 - 1850$ K, $X_{O_2} = 0.21$.

The results in this study further indicate that the proportion of mass loss due to nanoparticles decreases with increasing particle diameter, which aligns with the trend found in Cen et al. [59].

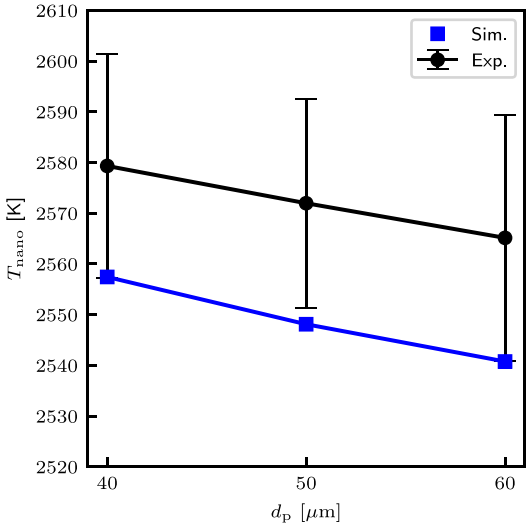

Fig. 11. The temperature T_{nano}, at which nanoparticle formation is initiated, in relation to the particle diameter.

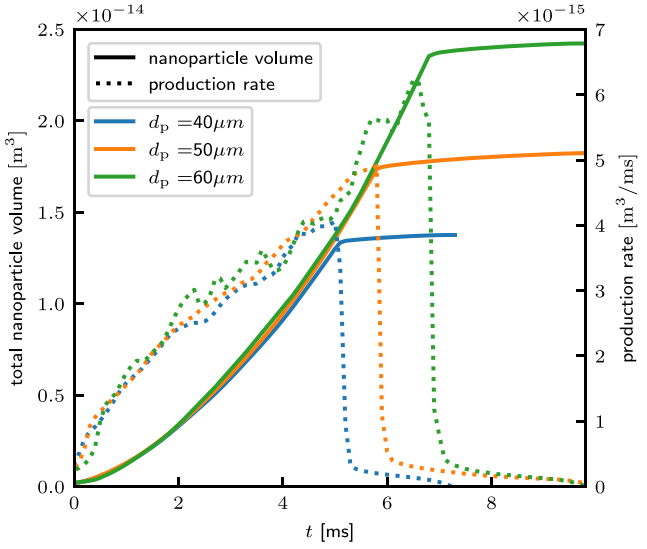

Fig. 12. Integrated nanoparticle volume over the entire domain, multiplied by 360 degrees, and formation rate over time. The curves are aligned at the onset of nanoparticle formation.

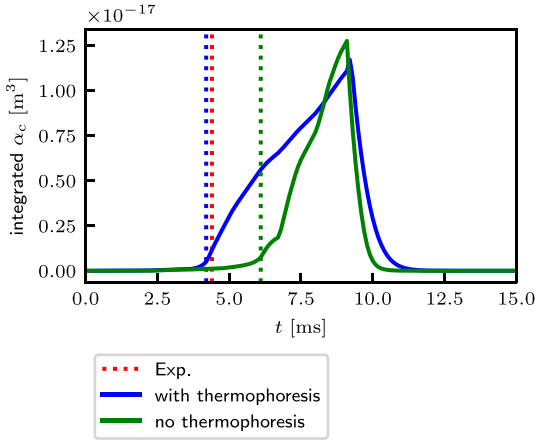

Fig. 13. Temporal evolution of the integrated nanoparticle volume for a case with thermophoresis and without thermophoresis (d_p = 40 µm). The vertical lines depict t_{nano}, whereby the red line shows the experimental t_{nano}.

4.4. Effect of thermophoresis and diffusiophoresis on the nanoparticle cloud

For nano-sized particles, e.g. soot [62–64] and alumina nanoparticles [20,21], thermophoretic transport is found to be just as important as convective transport. Diffusive transport is usually neglected for soot simulations [62–64]. For alumina nanoparticles, Gallier et al. [20] applied a size-independent diffusion coefficient on the nanoparticle phase and found that diffusiophoresis is negligible, while Finke and Sewerin [21] found size-dependent diffusive transport to be decisive for the shape of the nanoparticle cloud. For iron nanoparticles, Thijs et al. [18] included both thermophoresis and size-dependent diffusiophoresis, but the influence of these effects was not investigated in detail. The thermophoretic velocity is proportional to the temperature gradient and thus most likely becomes important in the boundary layer. Regarding diffusiophoresis, according to the Stokes–Einstein equation with the Cunningham correction factor [34], only particles with sizes smaller than around d_c = 10 nm experience non-negligible diffusiophoresis. While ex situ investigations suggest that iron nanoparticles have a size of around d_p = 45 nm [49], it is unclear, at which distance to the parent particle the nanoparticles accumulate to this size. Polydisperse simulation of iron nanoparticles suggests that nanoparticles that are smaller than 10 nm exist at a distance of < 250 µm from the parent particle [18]. In general, the data available on the size distribution of iron nanoparticles during the combustion of iron microparticles are scarce, which motivates the investigation of the effect of diffusiophoresis.

In this Section, the effect of thermophoresis and diffusiophoresis is investigated by successively excluding or including them from the simulation. For the investigation of thermophoresis, Case 4 is compared to Case 7. For the investigation of diffusiophoresis, Case 4 is compared to Case 8.

Fig. 13 shows the integrated nanoparticle volume for the reference case with thermophoresis, and for the case without thermophoresis. Additionally, respective times t_{nano} are indicated as vertical lines, whereby the experimental value is shown in red. It is observed that t_{nano} occurs considerably later in the case without thermophoresis, with a significant deviation from the experimental value. The peak value is slightly higher in the case without thermophoresis and the slope differs throughout the entire time. The differences become apparent in Fig. 14, where the distribution of the nanoparticle volume fraction is depicted. At t = 4.1 ms, t_{nano} of the reference case is passed, while t_{nano} of the case without thermophoresis is not yet reached. A distinct cloud has formed in the reference case, but in the case without thermophoresis, the amount of nanoparticles is much lower. An explanation is found by evaluating the thermophoresis and the convection velocity, along with the nanoparticle source in the boundary layer, depicted in Fig. 15. At t = 4.1 ms (early nanoparticle formation), the convection velocity points towards the particle, whereas the thermophoresis velocity points away from the particle. In the case with thermophoresis, although the net velocity is negative (towards the particle) in the first 30 µm around the particle, further away the net velocity is almost zero. At this distance, the condensation rate is still above zero, which means that nanoparticles, that are formed in this area, stay in place and accumulate. In contrast, in the absence of thermophoresis, the net velocity equals the convection velocity. Therefore, nanoparticles are pushed towards the particle surface, where they are not detected. In Fig. 14 at the time when the particle temperature reaches its peak (t_{peak}), it can be observed that the cloud in the case without thermophoresis is significantly smaller than the reference case. This can also be explained by the negative net velocity at the boundary layer. The most obvious difference between the two cases occurs after the nanoparticle formation stops. In Fig. 15 at t = 9.5 ms, the net velocity in the case with thermophoresis points away from the particle, which explains the formation of a halo around the particle after t_{peak} (Fig. 14). In the case without thermophoresis, the net velocity points towards the particle due to the negative Stefan flow velocity, which is caused by the

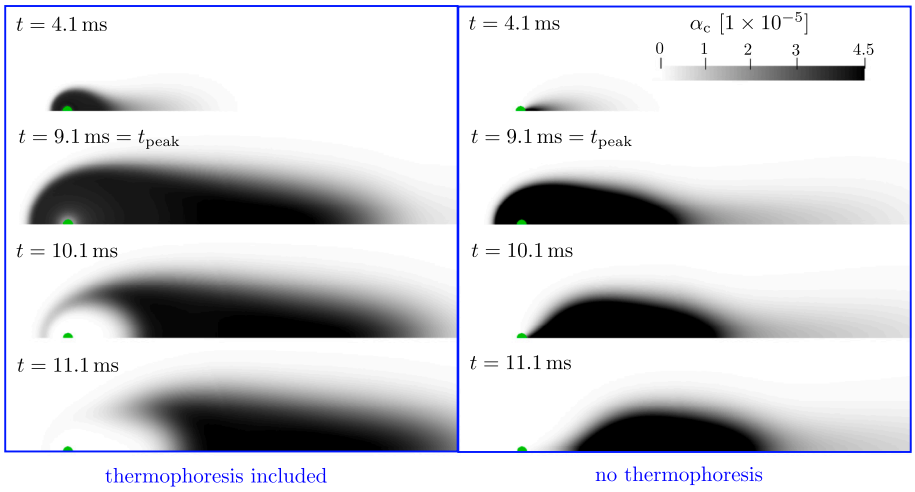

Fig. 14. Distribution of the nanoparticle volume fraction for a case with thermophoresis and a case without thermophoresis ($d_p = 40\,\mu m$).

O_2 consumption during reactive cooling. In consequence, the nanoparticles upstream and above the particle are transported in downstream direction, while the nanoparticles downstream of the particle stay in the vicinity of the surface for around 2 ms. While the experiment does not have DBI recordings after t_{peak} for this specific case, there are DBI recordings from other experiments [9,59], where a halo around the particle is clearly visible after termination of nanoparticle formation. Furthermore, the onset of the nanoparticle formation t_{nano} has a better agreement with the reference case. These indicate that thermophoresis is highly relevant for iron nanoparticle dynamics, which is in alignment with modeling approaches for soot and alumina nanoparticles [20,21,62–64].

For the investigation on the effect of diffusiophoresis, the diffusion coefficient in Eq. (3) is set to a constant value of $D_c = 1{\times}10^{-5}\,m^2/s$. This corresponds to particles with around $d_c = 3$ nm for gas temperatures between 1750 K and 2800 K [34]. Fig. 16 shows the nanoparticle cloud at t_{peak} for the reference case without diffusiophoresis and for the case with diffusiophoresis. It is obvious that the length of the cloud is significantly smaller with the influence of diffusiophoresis. This is due to the fact that nanoparticles diffuse to regions with lower concentrations instead of simply being transported downstream. To quantitatively evaluate the influence, the length and the growth rate of the cloud are compared in Fig. 17. Additionally, the relative velocity between the particle and the ambient gas is depicted to show the influence of convection. It is observed that the experimental growth rate correlates with the convection velocity in all cases. This is an indicator that the nanoparticle transport outside of the boundary layer, where Stefan flow and thermophoresis no longer have an influence, is dominated by convection. This is supported by the fact that the simulation without diffusiophoresis has a good agreement with the experiment regarding the nanoparticle cloud length. The growth rate without diffusiophoresis is slightly underpredicted, but it lies within the uncertainties of the relative velocity. In contrast, the case with diffusiophoresis significantly underpredicts the growth rate and the length of the nanoparticle cloud. Overall, it is shown that diffusiophoresis is negligible for most nanoparticles and that nanoparticles probably accumulate quickly from the smallest size to sizes above 10 nm. This justifies the assumption of $d_c = 45$ nm in Eq. (22).

An answer to **Q3** can be given as follows: Thermophoresis is highly relevant for the evolution of the nanoparticle cloud, while diffusiophoresis can be neglected.

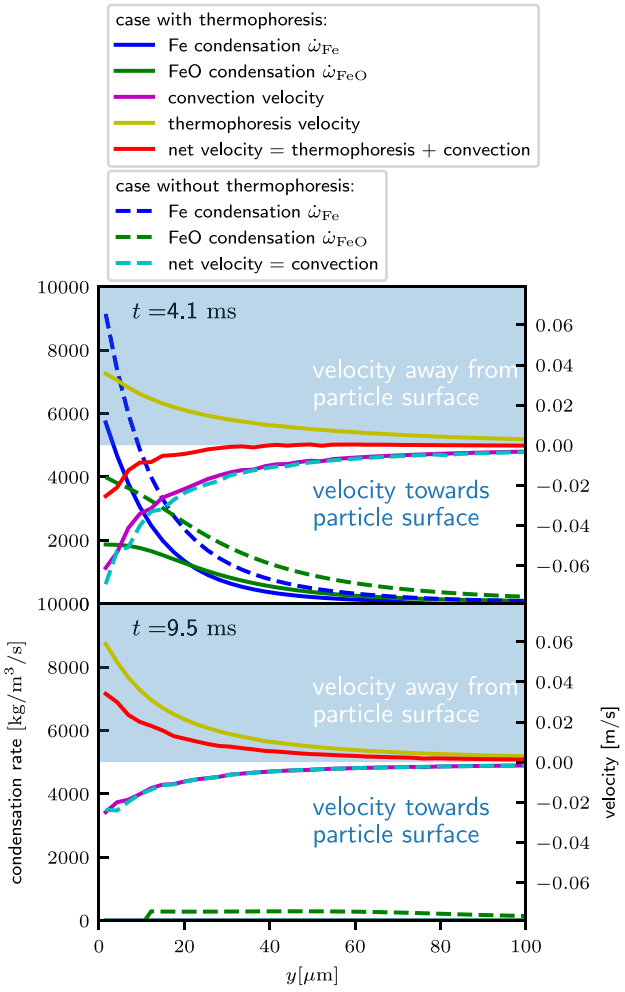

Fig. 15. Condensation rates, convection, and thermophoresis velocities along a line from the particle surface in radial direction for a particle with $d_p = 40\,\mu m$.

4.5. Effect of the evaporation model

In this Section, the evaporation model based on surface saturation (reference model, Section 3.3.2, Case 4) and the evaporation model from the HKS relation (Section 3.6, Case 9) are compared. Fig. 18 shows the evaporation rate and the integrated nanoparticle volume. For the HKS model, five simulations with sticking coefficients from 0.2 to 1 are conducted. It can be observed that lower sticking coefficients result in lower evaporation rates with increasing difference for decreasing ψ,

Fig. 16. Distribution of the nanoparticle volume fraction for a case without diffusiophoresis and a case with diffusiophoresis ($d_p = 40\,\mu m$).

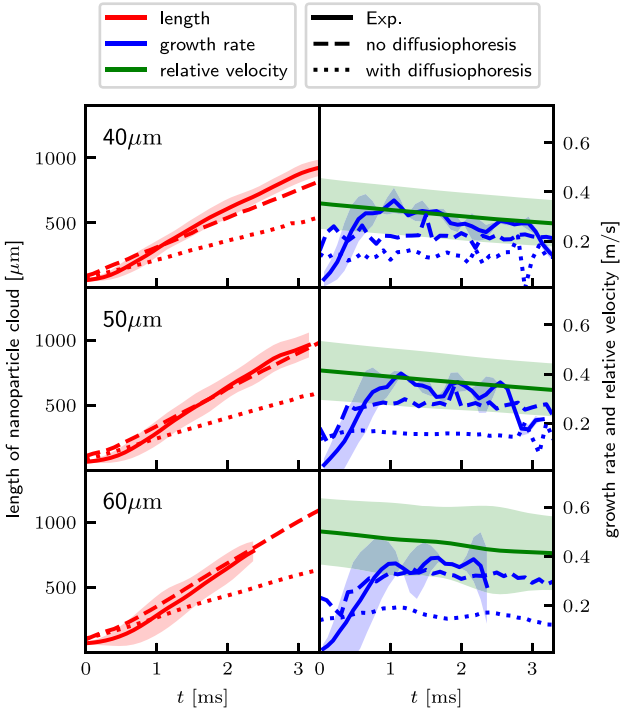

Fig. 17. Length and growth rate of the nanoparticle cloud, and the relative velocity between the particle and the ambient gas. Experimental values from the DBI recordings are compared with results from two numerical cases, one including diffusiophoresis and the other excluding it.

due to the non-linearity of the prefactor $2\psi/(2-\psi)$. The evaporation rates in the HKS model are in general lower than in the reference model. It should be mentioned that, if the particle temperature is computed with the enthalpy balance equation (Eq. (5)), lower evaporation rates would result in lower evaporation heat loss and thus, higher particle temperature. This in turn would increase the evaporation rate, such that the difference between the reference model and the HKS model would reduce. However, with identical temperature evolution, the HKS model predicts significantly lower evaporation rates. The difference is even more pronounced regarding the integrated nanoparticle volume. This is due to the fact that the reference model specifies the vapor pressure at the particle surface, thus reaching supersaturation as soon as the molecules are transported to lower temperature regions. In contrast, the partial pressure of Fe(g) at the surface in the HKS model approaches but never reaches the vapor pressure. Therefore, Fe(g) has to be transported further away from the particle to condense to nanoparticles. It can also be observed that t_{nano} is slightly shifted to a later time with decreasing sticking coefficients. Thus, there exists a sticking coefficient for which the experimental t_{nano} can be matched.

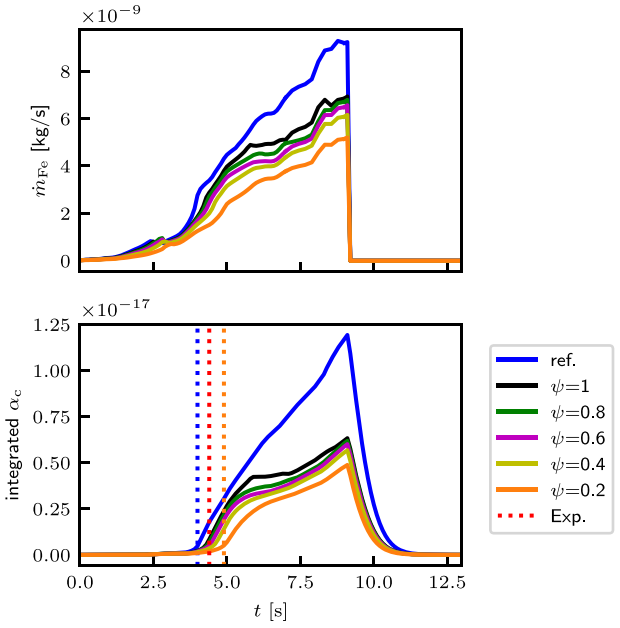

Fig. 18. Evaporation rate and integrated nanoparticle volume for a particle with $d_p = 40\,\mu m$ with the reference evaporation model (Section 3.3.2) and the HKS model (Section 3.6). For the HKS model, five sticking coefficients from $\psi = 0.2$ to $\psi = 1$ are compared. t_{nano} is depicted for the reference case, the experiment, and for the HKS model with $\psi = 0.2$.

Nevertheless, the difference in the integrated nanoparticle volume between the reference model and the HKS model is much larger than the difference in t_{nano}. Therefore, t_{nano} is not an appropriate indicator in this case. Due to the lack of quantitative experimental data for the amount of produced nanoparticles, it cannot be determined yet which model or which sticking coefficient is more accurate. However, this study shows that different choices for the modeling of evaporation lead to notably different predictions regarding the amount of formed nanoparticles, which answers **Q4**. This should be considered when a quantitative comparison with experimental data is pursued.

4.6. Sensitivity of nanoparticle formation to reaction mechanisms

In this Section, a qualitative comparison is drawn between the nanoparticle formation model by Thijs et al. [18], referred to as "reaction-driven", and the model introduced in Section 3.4, referred to as "condensation-driven". For both models, the simulations are conducted with the reaction mechanism in Table 1 ("Giesen reactions"), and the reaction mechanism in Table 3 ("Nanjaiah reactions"). The cases considered are 4, 10, 11, and 12. Fig. 19 shows the integrated volume fraction and the onset of nanoparticle formation. Between the reaction-driven model and the condensation-driven model, the onset of nanoparticle formation differs by around 0.7 ms. The reaction mechanism does not affect the onset significantly. For the maximum value of the nanoparticle volume, it is observed that there is a minor sensitivity to the reaction mechanism in the condensation-driven model. In this model, condensation and reaction are competing against each other and it appears that condensation is the dominant mechanism. Unlike gas phase reactions that are driven by kinetics, condensation is governed by vapor pressure, a thermodynamic state variable. In contrast, the sensitivity in the reaction-driven model to the reaction mechanism is more pronounced, since the formation rate is directly determined by the reaction rate. Therefore, caution must be taken when applying the reaction-driven model, since reaction mechanisms for very high temperatures are subject to considerable uncertainty. It is worth mentioning that the reactions by Giesen et al. [46] were developed in a

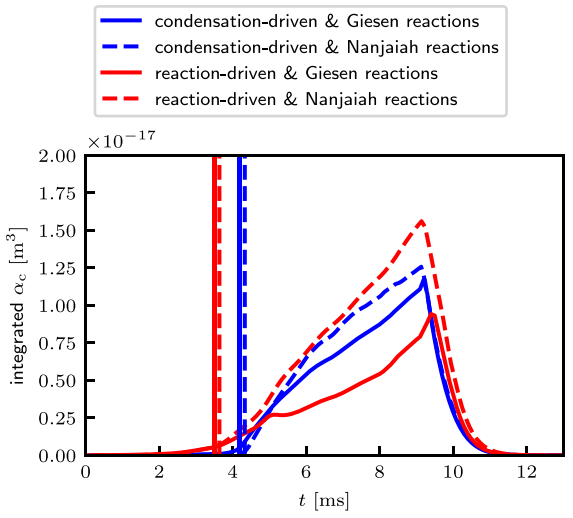

Fig. 19. Temporal evolution of the integrated nanoparticle volume for a particle with $d_p = 40\,\mu m$ with different nanoparticle formation models and different reaction mechanisms. The vertical lines depict t_{nano}.

hydrogen-free atmosphere, and the "Nanjaiah reactions" were modified by Thijs et al. [18] to exclude hydrogen. In the current configuration, which contains hydrogen-species, the original mechanism by Nanjaiah et al. [23] might be more appropriate. This hypothesis is tested by employing the original mechanism with results shown in Appendix. Fig. A.20 in the appendix shows that, despite a change in the peak value, the major characteristics of the integrated nanoparticle volume remain unchanged. Thus, the conclusions are invariant, regardless of whether the original mechanism by Nanjaiah et al. [23] or the modified one by Thijs et al. [18] is employed.

Question **Q5** can be answered as follows: The gas phase reactions do not affect the onset of nanoparticle formation, but they can affect the amount of nanoparticles formed. While the condensation-driven model shows a minor sensitivity to gas phase reactions, the reaction-driven model shows a considerable sensitivity.

5. Conclusions

In this study, boundary layer resolved simulations of single iron microparticles are conducted to explore the nanoparticle formation during combustion. The developed nanoparticle formation model considers condensation as the nucleation mechanism. Numerically obtained particle temperature profiles and characteristics of the nanoparticle cloud are compared with experimental measurements. The conclusions from the present study are:

1. **The particle temperature is decisive in the prediction of nanoparticle formation.** The utilized particle model reproduces the peak temperature, but notable deviations still exist in the temperature profiles between simulation and experiment. Prescribing the measured particle temperature evolution in the simulation, the onset temperature of nanoparticle formation is predicted well.
2. **The relevant transport processes for the nanoparticle cloud evolution are convection and thermophoresis.** The characteristics of the predicted nanoparticle cloud show a good agreement with the experiments. Most nanoparticles are not affected by diffusiophoresis.
3. **The evaporation model has a significant effect on the amount of produced nanoparticles.** An assessment of the evaporation model requires quantitative measurements of the amount of nanoparticles, which are not yet available.
4. **The gas phase reactions do not affect the onset of nanoparticle formation, but the amount of formed nanoparticles.** The present nanoparticle formation model considers condensation as the nucleating mechanism and it is compared to a model that considers a chemical reaction (to Fe_2O_3(s)) as the nucleating mechanism [18]. Both models predict nanoparticle volume fractions in a similar order of magnitude. It is also found that the sensitivity of the nanoparticle formation rate in the condensation-driven model is almost insensitive to the gas phase reaction mechanism.

Our study highlights that further reference datasets of nanoparticle formation are crucially needed. For more extensive quantitative comparisons between simulation and experiment, future research could address (1) in situ measurements of the nanoparticle volume fraction or their total mass and (2) models to describe the polydispersity of the formed nanoparticles. Future work should extend the modeling approach to include the oxidation of FeO nanoparticles to Fe_2O_3 and also consider a reaction-driven pathway to nanoparticle formation.

Following the first conclusion of this study, future designs for industrial reactors should aim to find a compromise between energy output and particle temperature, since decreasing the particle temperature would mitigate nanoparticle formation. This could be achieved by either decreasing the ambient temperature or the oxygen concentration.

CRediT authorship contribution statement

Bich-Diep Nguyen: Writing – review & editing, Writing – original draft, Visualization, Validation, Methodology, Investigation, Data curation, Conceptualization, Formal analysis. **Arne Scholtissek:** Writing – review & editing, Supervision, Project administration, Conceptualization, Formal analysis. **Tao Li:** Writing – review & editing, Visualization, Data curation, Investigation, Formal analysis, Methodology. **Daoguan Ning:** Writing – review & editing, Data curation. **Oliver Thomas Stein:** Writing – review & editing, Resources. **Andreas Dreizler:** Writing – review & editing, Funding acquisition. **Christian Hasse:** Writing – review & editing, Project administration, Funding acquisition, Conceptualization.

Declaration of competing interest

The authors declare that they have no known competing financial interests or personal relationships that could have appeared to influence the work reported in this paper.

Acknowledgments

The authors are grateful to L. Thijs and Dr. Y. Shoshin for the fruitful discussions on this study and to T. D. Luu for helpful advice in the development of the numerical setup.

This work was funded by the Hessian Ministry of Higher Education, Research, Science and the Arts, Germany - cluster project Clean Circles. O. T. Stein acknowledges the financial support by the Boysen foundation, Germany, project BOY-195.

The authors gratefully acknowledge the computing time provided to them on the high-performance computer Lichtenberg at the NHR Center NHR4CES at TU Darmstadt (project number p0020731). This is funded by the Federal Ministry of Education and Research, Germany, and the state governments participating on the basis of the resolutions of the GWK for national high performance computing at universities (www.nhr-verein.de/unsere-partner).

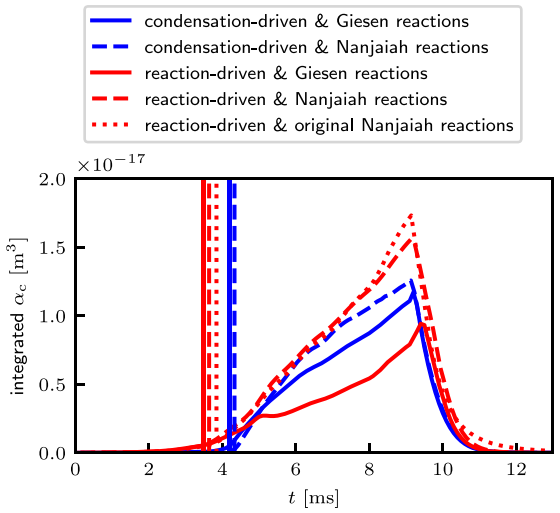

Fig. A.20. Temporal evolution of the integrated nanoparticle volume for a particle with $d_p = 40\,\mu m$ with different nanoparticle formation models and different reaction mechanisms. The vertical lines depict t_{nano}.

Appendix. Reaction mechanism including hydrogen-containing species

Following the discussion in Section 4.6, Fig. A.20 shows the integrated nanoparticle volume fraction over time from the simulation with the original mechanism by Nanjaiah et al. [23] including hydrogen-containing species ("original Nanjaiah reactions"), and the modified mechanism by Thijs et al. [18] ("Nanjaiah reactions"). The results are depicted in comparison to the results already shown in Section 4.6. At the peak, the original Nanjaiah mechanism differs by 11% from the modified Nanjaiah mechanism. However, the characteristics remain the same.

Data availability

Data will be made available on request.

References

[1] J.M. Bergthorson, Recyclable metal fuels for clean and compact zero-carbon power, Prog. Energy Combust. Sci. 68 (2018) 169–196.
[2] P. Debiagi, R. Rocha, A. Scholtissek, J. Janicka, C. Hasse, Iron as a sustainable chemical carrier of renewable energy: Analysis of opportunities and challenges for retrofitting coal-fired power plants, Renew. Sustain. Energy Rev. 165 (2022) 112579.
[3] J. Bergthorson, S. Goroshin, M. Soo, P. Julien, J. Palecka, D. Frost, D. Jarvis, Direct combustion of recyclable metal fuels for zero-carbon heat and power, Appl. Energy 160 (2015) 368–382.
[4] P. Tóth, Y. Ögren, A. Sepman, P. Gren, H. Wiinikka, Combustion behavior of pulverized sponge iron as a recyclable electrofuel, Powder Technol. 373 (2020) 210–219.
[5] S. Li, J. Huang, W. Weng, Y. Qian, X. Lu, M. Aldén, Z. Li, Ignition and combustion behavior of single micron-sized iron particle in hot gas flow, Combust. Flame 241 (2022) 112099.
[6] D. Ning, Y. Shoshin, M. van Stiphout, J. van Oijen, G. Finotello, P. de Goey, Temperature and phase transitions of laser-ignited single iron particle, Combust. Flame 236 (2022) 111801.
[7] D. Ning, Y. Shoshin, J. van Oijen, G. Finotello, L. de Goey, Burn time and combustion regime of laser-ignited single iron particle, Combust. Flame 230 (2021) 111424.
[8] D. Ning, Y. Shoshin, J.A. van Oijen, G. Finotello, L. de Goey, Critical temperature for nanoparticle cloud formation during combustion of single micron-sized iron particle, Combust. Flame 244 (2022) 112296.
[9] T. Li, F. Heck, F. Reinauer, B. Böhm, A. Dreizler, Visualizing particle melting and nanoparticle formation during single iron particle oxidation with multi-parameter optical diagnostics, Combust. Flame 245 (2022) 112357.
[10] D. Wen, Nanofuel as a potential secondary energy carrier, Energy & Environ. Sci. 3 (5) (2010) 591–600.
[11] K. Donaldson, L. Tran, L.A. Jimenez, R. Duffin, D.E. Newby, N. Mills, W. MacNee, V. Stone, Combustion-derived nanoparticles: A review of their toxicology following inhalation exposure, Part. Fibre Toxicol. 2 (1) (2005) 10.
[12] J. Lee, A. Tomboulides, S. Orszag, R. Yetter, F. Dryer, A transient two-dimensional chemically reactive flow model: Fuel particle combustion in a nonquiescent environment, Symp. (International) Combust. 26 (2) (1996) 3059–3065.
[13] P. Nikrityuk, M. Gräbner, M. Kestel, B. Meyer, Numerical study of the influence of heterogeneous kinetics on the carbon consumption by oxidation of a single coal particle, Fuel 114 (2013) 88–98.
[14] G. Tufano, O. Stein, A. Kronenburg, A. Frassoldati, T. Faravelli, L. Deng, A. Kempf, M. Vascellari, C. Hasse, Resolved flow simulation of pulverized coal particle devolatilization and ignition in air- and O 2 /CO 2 -atmospheres, Fuel 186 (2016) 285–292.
[15] G.L. Tufano, O.T. Stein, A. Kronenburg, G. Gentile, A. Stagni, A. Frassoldati, T. Faravelli, A.M. Kempf, M. Vascellari, C. Hasse, Fully-resolved simulations of coal particle combustion using a detailed multi-step approach for heterogeneous kinetics, Fuel 240 (2019) 75–83.
[16] M. Vascellari, H. Xu, C. Hasse, Flamelet modeling of coal particle ignition, Proc. Combust. Inst. 34 (2) (2013) 2445–2452.
[17] Z. Wu, G. Ou, Y. Ren, H. Jin, L. Guo, Particle-resolved numerical study of the forced convection heat transfer characteristics of an endothermic-biomass particle placed in supercritical water crossflow, Renew. Energy 158 (2020) 271–279.
[18] L.C. Thijs, C.E.A.G. van Gool, W.J.S. Ramaekers, J.A. van Oijen, L.P.H. de Goey, Resolved simulations of single iron particle combustion and the release of nano-particles, Proc. Combust. Inst. 39 (3) (2023) 3551–3559.
[19] M.W. Beckstead, Y. Liang, K. Pudduppakkam, Numerical simulation of single aluminum particle combustion, Combust. Explos. Shock. Waves 41 (2005) 622–638.
[20] S. Gallier, A. Braconnier, F. Godfroy, F. Halter, C. Chauveau, The role of thermophoresis on aluminum oxide lobe formation, Combust. Flame 228 (2021) 142–153.
[21] J. Finke, F. Sewerin, A population balance approach for predicting the size distribution of oxide smoke near a burning aluminum particle, Combust. Flame 265 (2024) 113464.
[22] I. Wlokas, A. Faccinetto, B. Tribalet, C. Schulz, A. Kempf, Mechanism of iron oxide formation from iron pentacarbonyl-doped low-pressure hydrogen/oxygen flames, Int. J. Chem. Kinet. 45 (8) (2013) 487–498.
[23] M. Nanjaiah, A. Pilipodi-Best, M.R. Lalanne, P. Fjodorow, C. Schulz, S. Cheskis, A. Kempf, I. Wlokas, I. Rahinov, Experimental and numerical investigation of iron-doped flames: FeO formation and impact on flame temperature, Proc. Combust. Inst. 38 (1) (2021) 1249–1257.
[24] Y. Karakaya, S. Kluge, H. Wiggers, C. Schulz, T. Kasper, Investigation of the combustion of iron pentacarbonyl and the formation of key intermediates in iron oxide synthesis flames, Chem. Eng. Sci. 230 (2021) 116169.
[25] A. Panahi, D. Chang, M. Schiemann, A. Fujinawa, X. Mi, J.M. Bergthorson, Y.A. Levendis, Combustion behavior of single iron particles-part i: An experimental study in a drop-tube furnace under high heating rates and high temperatures, Appl. Energy Combust. Sci. 13 (2023) 100097.
[26] H. Wiinikka, T. Vikström, J. Wennebro, P. Toth, A. Sepman, Pulverized sponge iron, a zero-carbon and clean substitute for fossil coal in energy applications, Energy & Fuels 32 (9) (2018) 9982–9989.
[27] J. Palečka, J. Sniatowsky, S. Goroshin, A.J. Higgins, J.M. Bergthorson, A new kind of flame: Observation of the discrete flame propagation regime in iron particle suspensions in microgravity, Combust. Flame 209 (2019) 180–186.
[28] T. Li, B.-D. Nguyen, Y. Gao, D. Ning, B. Böhm, A. Scholtissek, A.C.T. van Duin, C. Hasse, A. Dreizler, Critical nanoparticle formation in iron combustion: single particle experiments with in-situ multi-parameter diagnostics aided by multi-scale simulations (Preprint), 2024.
[29] T. Li, P. Farmand, C. Geschwindner, M. Greifenstein, J. Köser, C. Schumann, A. Attili, H. Pitsch, A. Dreizler, B. Böhm, Homogeneous ignition and volatile combustion of single solid fuel particles in air and oxy-fuel conditions, Fuel 291 (2021) 120101.
[30] D.G. Goodwin, H.K. Moffat, I. Schoegl, R.L. Speth, B.W. Weber, Cantera: An object-oriented software toolkit for chemical kinetics, thermodynamics, and transport processes, 2022.
[31] T. Hazenberg, J. van Oijen, Structures and burning velocities of flames in iron aerosols, Proc. Combust. Inst. 38 (3) (2021) 4383–4390.
[32] X. Mi, A. Fujinawa, J.M. Bergthorson, A quantitative analysis of the ignition characteristics of fine iron particles, Combust. Flame 240 (2022) 112011.
[33] J. Mich, A.K. da Silva, D. Ning, T. Li, D. Raabe, B. Böhm, A. Dreizler, C. Hasse, A. Scholtissek, Modeling the oxidation of iron microparticles during the reactive cooling phase, Proc. Combust. Inst. 40 (1–4) (2024) 105538.
[34] S. Friendlander, Smoke, Dust and Haze: Fundamentals of Aerosol Dynamics, vol. 20, Ox-ford University Press, New York, USA, 2000.

[35] M. Muller, H. El-Rabii, R. Fabbro, Liquid phase combustion of iron in an oxygen atmosphere, J. Mater. Sci. 50 (2015) 3337–3350.
[36] B.J. McBride, NASA Glenn Coefficients for Calculating Thermodynamic Properties of Individual Species, National Aeronautics and Space Administration, John H. Glenn Research Center at Lewis Field, 2002.
[37] J.-O. Andersson, T. Helander, L. Höglund, P. Shi, B. Sundman, Thermo-calc & DICTRA, computational tools for materials science, CALPHAD 26 (2) (2002) 273–312.
[38] M.W. Chase, N. I. S. O. (US), NIST-JANAF Thermochemical Tables, vol. 9, American Chemical Society Washington, DC, 1998.
[39] Y.S. Touloukian, Recommended Values of the Thermophysical Properties of Eight Alloys, Major Constituents and their Oxides, Purdue University, Thermophysical Propeties Research Center, 1966.
[40] A. Kirshenbaum, J. Cahill, The density of liquid iron from the melting point to 2500 K, Trans. Met. Soc. AIME 224 (1962).
[41] M. Takeda, T. Onishi, S. Nakakubo, S. Fujimoto, Physical properties of iron-oxide scales on si-containing steels at high temperature, Mater. Trans. 50 (9) (2009) 2242–2246.
[42] F. Millot, J.-C. Rifflet, G. Wille, V. Sarou-Kanian, Density and surface tension of liquid iron oxides, High Temp. - High Press. 38 (3) (2009).
[43] A. Fujinawa, L.C. Thijs, J. Jean-Philyppe, A. Panahi, D. Chang, M. Schiemann, Y.A. Levendis, J.M. Bergthorson, X. Mi, Combustion behavior of single iron particles, part ii: A theoretical analysis based on a zero-dimensional model, Appl. Energy Combust. Sci. 14 (2023) 100145.
[44] C.E.A.G. van Gool, L.C. Thijs, W.J.S. Ramaekers, J.A. van Oijen, L.P.H. de Goey, Particle equilibrium composition model for iron dust combustion, Appl. Energy Combust. Sci. 13 (2023) 100115.
[45] J. Finke, F. Sewerin, Combining a population balance approach with detailed chemistry to model the condensation of oxide smoke during aluminum combustion in spatially homogeneous reactors, Combust. Flame 248 (2023) 112510.
[46] A. Giesen, D. Woiki, J. Herzler, P. Roth, Fe atoms by O2 based on Fe- and O-concentration measurements, Proc. Combust. Inst. 29 (1) (2002) 1345–1352.
[47] M. Rumminger, D. Reinelt, V. Babushok, G.T. Linteris, Numerical study of the inhibition of premixed and diffusion flames by iron pentacarbonyl, Combust. Flame 116 (1–2) (1999) 207–219.
[48] W.M. Haynes, CRC Handbook of Chemistry and Physics, ninety fifth ed., 2014.
[49] S. Buchheiser, M.P. Deutschmann, F. Rhein, A. Allmang, M. Fedoryk, B. Stelzner, S. Harth, D. Trimis, H. Nirschl, Particle and phase analysis of combusted iron particles for energy storage and release, Materials 16 (5) (2023) 2009.
[50] D.H. Huang, T.N. Tran, B. Yang, Investigation on the reaction of iron powder mixture as a portable heat source for thermoelectric power generators, J. Therm. Anal. Calorim. 116 (2) (2014) 1047–1053.
[51] L. Cifuentes, J. Sellmann, I. Wlokas, A. Kempf, Direct numerical simulations of nanoparticle formation in premixed and non-premixed flame–vortex interactions, Phys. Fluids 32 (9) (2020) 093605.
[52] M.K. King, Modeling of single particle aluminum combustion in CO2- N2 atmospheres, Symp. (International) Combust. 17 (1) (1979) 1317–1328.
[53] B.T. Bojko, P.E. DesJardin, E.B. Washburn, On modeling the diffusion to kinetically controlled burning limits of micron-sized aluminum particles, Combust. Flame 161 (12) (2014) 3211–3221.
[54] H. Hertz, Ueber die Verdunstung der Flüssigkeiten, insbesondere des Quecksilbers, im luftleeren Raume, Ann. Phys., Lpz. 253 (10) (1882) 177–193.
[55] M. Knudsen, Die maximale Verdampfungsgeschwindigkeit des Quecksilbers, Ann. Phys., Lpz. 352 (13) (1915) 697–708.
[56] R.W. Schrage, A theoretical study of interphase mass transfer, 1953.
[57] J. Glorian, S. Gallier, L. Catoire, On the role of heterogeneous reactions in aluminum combustion, Combust. Flame 168 (2016) 378–392.
[58] L.C. Thijs, M.-A. Van Ende, J.A. van Oijen, P. de Goey, X. Mi, A numerical study of internal transport in oxidizing liquid core–shell iron particles, Combust. Flame 271 (2025) 113826.
[59] L. Cen, Z. Lyu, Y. Qian, Z. Li, X. Lu, In-situ light extinction nano-oxide volume fraction measurements during single iron particle combustion, Proc. Combust. Inst. 40 (1–4) (2024) 105305.
[60] D. Ning, A. Dreizler, A quantitative theory for heterogeneous combustion of nonvolatile metal particles in the diffusion-limited regime, Combust. Flame 269 (2024) 113692.
[61] N. Poletaev, M. Khlebnikova, Combustion of iron particles suspension in laminar premixed and diffusion flames, Combust. Sci. Technol. 194 (7) (2022) 1356–1377.
[62] L. Zimmer, F.M. Pereira, J.A. van Oijen, L.P.H. de Goey, Investigation of mass and energy coupling between soot particles and gas species in modelling ethylene counterflow diffusion flames, Combust. Theory Model. 21 (2) (2017) 358–379.
[63] F. Bisetti, G. Blanquart, M.E. Mueller, H. Pitsch, On the formation and early evolution of soot in turbulent nonpremixed flames, Combust. Flame 159 (1) (2012) 317–335.
[64] I.M. Kennedy, W. Kollmann, J.-Y. Chen, A model for soot formation in a laminar diffusion flame, Combust. Flame 81 (1) (1990) 73–85.